

X-ray constraints on the fraction of obscured AGN at high accretion luminosities

A. Georgakakis^{1,2*}, M. Salvato¹, Z. Liu^{3,4}, J. Buchner^{1,5,6}, W. N. Brandt^{7,8,9},
T. Tasnim Ananna¹⁰, A. Schulze¹¹, Yue Shen^{12,13}, S. LaMassa¹⁴, K. Nandra¹,
A. Merloni¹, I. D. McGreer¹⁵

¹Max Planck Institut für Extraterrestrische Physik, Giessenbachstraße, 85748 Garching, Germany

²National Observatory of Athens, V. Paulou & I. Metaxa, 11532, Greece

³National Astronomical Observatories, Chinese Academy of Sciences, Beijing 100012, People's Republic of China

⁴University of Chinese Academy of Sciences, Beijing 100049, People's Republic of China

⁵Millennium Institute of Astrophysics, Vicuña. MacKenna 4860, 7820436 Macul, Santiago, Chile

⁶Pontificia Universidad Católica de Chile, Instituto de Astrofísica, Casilla 306, Santiago 22, Chile

⁷Department of Astronomy and Astrophysics, 525 Davey Lab, The Pennsylvania State University, University Park, PA 16802, USA

⁸Institute for Gravitation and the Cosmos, The Pennsylvania State University, University Park, PA 16802, USA

⁹Department of Physics, 104 Davey Laboratory, The Pennsylvania State University, University Park, PA 16802, USA

¹⁰Department of Physics, Yale University, New Haven, CT 06520-8120, P.O. Box 208120, USA

¹¹Kavli IPMU (WPI), UTIAS, The University of Tokyo, Kashiwa, Chiba 277-8583, Japan

¹²Department of Astronomy, University of Illinois at Urbana-Champaign, Urbana, IL 61801, USA

¹³National Center for Supercomputing Applications, University of Illinois at Urbana-Champaign, Urbana, IL 61801, USA

¹⁴NASA Goddard Space Flight Center, Greenbelt, MD, USA

¹⁵Steward Observatory, The University of Arizona, 933 North Cherry Avenue, Tucson, AZ 85721-0065, USA

Accepted XXX. Received YYY; in original form ZZZ

ABSTRACT

The wide-area XMM-XXL X-ray survey is used to explore the fraction of obscured AGN at high accretion luminosities, $L_X(2 - 10 \text{ keV}) \gtrsim 10^{44} \text{ erg s}^{-1}$, and out to redshift $z \approx 1.5$. The sample covers an area of about 14 deg^2 and provides constraints on the space density of powerful AGN over a wide range of neutral hydrogen column densities extending beyond the Compton-thick limit, $N_H \approx 10^{24} \text{ cm}^{-2}$. The fraction of obscured Compton-thin ($N_H = 10^{22} - 10^{24} \text{ cm}^{-2}$) AGN is estimated to be ≈ 0.35 for luminosities $L_X(2 - 10 \text{ keV}) > 10^{44} \text{ erg s}^{-1}$ independent of redshift. For less luminous sources the fraction of obscured Compton-thin AGN increases from 0.45 ± 0.10 at $z = 0.25$ to 0.75 ± 0.05 at $z = 1.25$. Studies that select AGN in the infrared via template fits to the observed Spectral Energy Distribution of extragalactic sources estimate space densities at high accretion luminosities consistent with the XMM-XXL constraints. There is no evidence for a large population of AGN (e.g. heavily obscured) identified in the infrared and missed at X-ray wavelengths. We further explore the mid-infrared colours of XMM-XXL AGN as a function of accretion luminosity, column density and redshift. The fraction of XMM-XXL sources that lie within the mid-infrared colour wedges defined in the literature to select AGN is primarily a function of redshift. This fraction increases from about 20-30% at $z=0.25$ to about 50-70% at $z = 1.5$.

Key words: galaxies: active, galaxies: Seyfert, quasars: general, X-rays: diffuse background

1 INTRODUCTION

It is now well established that the dominant fraction of the growth of supermassive black holes at the centres of galax-

ies is taking place behind dense dust and gas obscuring cloud. The black hole mass density estimated by integrating the luminosity function of unobscured UV/optically-selected QSOs for example, falls short of the local black hole mass function (e.g. Soltan 1982; Marconi et al. 2004; Merloni & Heinz 2008). Under the assumption that the dominant mode

* E-mail: age@mpe.mpg.de

of black hole growth is accretion, this implies large numbers of obscured Active Galactic Nuclei (AGN) that are missing from UV/optical surveys. This is also supported by studies of the composition of the diffuse X-ray background radiation (XRB) that represents the integrated emission of AGN over cosmic time. A large fraction of obscured AGN, including some deeply buried ones, are needed to synthesise the observed XRB spectrum in the energy interval $\approx 2 - 100$ keV (e.g. Comastri et al. 1995; Worsley et al. 2005; Gilli et al. 2007; Draper & Ballantyne 2009; Akylas et al. 2012). Observational constraints on the distribution of the obscuration level for AGN are therefore essential to understand in detail the accretion history of the Universe and also compile unbiased AGN samples to explore the relation between black hole growth and galaxy evolution (e.g. Brandt & Alexander 2015).

X-ray spectroscopy provides a direct measure of the line-of-sight gas obscuration of AGN, parametrised by the equivalent column density of neutral hydrogen, N_H . As a result, high-energy observations have been used extensively to estimate the fraction of obscured AGN as a function of redshift and accretion luminosity. Follow-up observations of local AGN samples selected in the mid-IR (Brightman & Nandra 2011b,a), hard X-rays (Burlon et al. 2011; Ajello et al. 2012) or via nuclear optical emission lines (Risaliti et al. 1999; Panessa et al. 2006; Akylas & Georgantopoulos 2009), measure obscured ($N_H > 10^{22}$ cm $^{-2}$) AGN fractions of $\approx 60\%$. These studies also find a population of deeply buried sources with hydrogen column densities above the Thomson scattering limit ($N_H \gtrsim 10^{24}$ cm $^{-2}$; Compton-thick), which represent $\approx 30 - 50\%$ of the overall obscured population.

Outside the local Universe *XMM-Newton*, *Chandra* (e.g. Ueda et al. 2003; Barger et al. 2005; Della Ceca et al. 2008; Yencho et al. 2009; Ebrero et al. 2009; Ueda et al. 2014; Aird et al. 2015a; Buchner et al. 2015) and more recently *NuSTAR* (Alexander et al. 2013; Aird et al. 2015b) surveys provide a rich dataset for studies of the obscuration distribution of AGN. Nuclear obscuration has been shown to be less common among powerful AGN (Akylas et al. 2006; Tozzi et al. 2006; Hasinger 2008; Ebrero et al. 2009; Ueda et al. 2014), possibly indicating the impact of black hole related outflows, which sweep away gas and dust clouds in luminous sources (Silk & Rees 1998; Fabian 1999; King 2003). At low accretion luminosities there is also evidence for a decrease in the incidence of obscuration among AGN (e.g. Brightman & Nandra 2011b; Burlon et al. 2011; Buchner et al. 2015), a trend which may relate to the efficiency of cloud formation when the radiative output of accreting supermassive black holes drops below a certain limit. The obscured AGN fraction integrated over accretion luminosity may also increase with redshift at least out to $z \approx 1.5 - 2$ (e.g. La Franca et al. 2005; Vito et al. 2014; Buchner et al. 2015), a trend which may be linked to the overall increase of the gas and dust content of galaxies at earlier epochs (Dunne et al. 2011; Magdis et al. 2012; Tacconi et al. 2013). The number of Compton-thick sources among AGN is still debated with different studies finding discrepant results in terms of both space density and cosmological evolution (e.g. Brightman & Ueda 2012; Ueda et al. 2014; Buchner et al. 2015; Akylas et al. 2016).

Current results on the obscuration distribution of AGN

outside the local Universe are largely based on relatively small area and deep X-ray surveys. Because of the form of the X-ray luminosity function, these datasets are dominated by low and moderate luminosity sources. Constraints at high accretion luminosities, close to and above the knee of the X-ray luminosity function ($L_X(2 - 10$ keV) $\approx 10^{44}$ erg s $^{-1}$ Aird et al. 2010), are therefore affected by Poisson noise. There are for example, only 14 AGN with $L_X(2 - 10$ keV) $> 10^{44}$ erg s $^{-1}$ and $z < 1$ in the deep *Chandra* survey source catalogues compiled by Georgakakis et al. (2015). Because bright sources are rare, wide-area surveys are required for statistically large samples. Such luminous sources are important as they dominate the accretion history of the Universe and may also represent an interesting phase of black hole growth, when AGN feedback processes are sufficiently violent to have an impact on the evolution of their host galaxies (e.g. Hopkins et al. 2006). Despite the large number of deep and relatively small area ($\lesssim 2$ deg 2) X-ray surveys carried out by *Chandra* or *XMM-Newton* (Brandt & Alexander 2015), there are currently only a few wide-area X-ray samples. These include the *Chandra* survey in the Boötes field (XBoötes, ≈ 9 deg 2 ; Kenter et al. 2005; Brand et al. 2006), the XMM-XXL ($\approx 2 \times 25$ deg 2 ; Pierre et al. 2015) and the X-ray Survey in SDSS Stripe 82 (Stripe82X, 31 deg 2 of which ≈ 16 deg 2 is contiguous; LaMassa et al. 2016).

In this paper we present results on the obscuration distribution of luminous [$L_X(2 - 10$ keV) $\gtrsim 10^{44}$ erg s $^{-1}$] AGN to $z \approx 1.5$ using one of the largest contiguous X-ray surveys to date, the XMM-XXL (Pierre et al. 2015). This dataset, like any X-ray selected sample, includes sources with a small number of photons. This poses a challenge to studies that attempt to infer AGN parameters, such as level of line-of-sight obscuration or accretion luminosity, by modeling their X-ray spectra. In our work we address this issue by making realistic assumptions on the adopted X-ray spectral models and using robust statistical methods for unbiased estimates of X-ray spectral parameters and their associated uncertainties. We show that the XMM-XXL despite its relatively shallow depth (typically 10 ks per *XMM* pointing) provides new measurements of the AGN space density at luminosities $L_X(2 - 10$ keV) $\gtrsim 10^{44}$ erg s $^{-1}$ over a wide range of line-of-sight hydrogen column densities extending above the Compton-thick limit. Surveys like the XMM-XXL, in terms of depth and area, provide an excellent complement to deep X-ray samples for characterising the statistical properties of AGN over a wide luminosity and obscuration baselines. In the calculations that follow we adopt cosmological parameters $H_0 = 70$ km s $^{-1}$ Mpc $^{-1}$, $\Omega_M = 0.3$, $\Omega_\Lambda = 0.7$.

2 DATA ANALYSIS AND PRODUCTS

2.1 X-ray source catalogue

The X-ray source catalogue used in this paper is extracted from the equatorial field ($\alpha \approx 2^h 16^m$, $\delta \approx -4^\circ 52'$) of the XMM-XXL survey (Pierre et al. 2015) following the X-ray data reduction and analysis steps described in Liu et al. (2016). In the rest of this paper we refer to the equatorial subregion of the XMM-XXL presented by Liu et al. (2016) as XMM-XXL-N. The most important details of the X-ray data analysis methodology are outlined below.

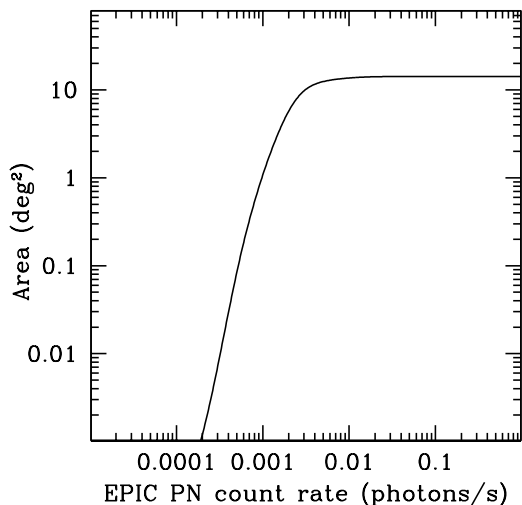


Figure 1. XMM-XXL-N survey area (y-axis) sensitive to sources of a given EPIC PN count rate in the 2-8 keV energy band (x-axis). In the sensitivity map calculation only the part of the XMM-XXL-N that overlaps with the Canada-France Hawaii Telescope Lensing Survey (CFHTLenS; Heymans et al. 2012; Erben et al. 2013) is used (total of about 14 deg²). The area of the XMM-XXL-N survey that lies either outside the CFHTLenS footprint or within the CFHTLenS masked regions associated with optically bright stars is excluded (about 5 deg²). This is because the CFHTLenS is used for the identification of XMM-XXL-N sources with optical counterparts (see Section 2.2).

For the reduction of the *XMM* observations of the equatorial XXL field the *XMM* Science Analysis System (SAS) version 12 is used. Event files for the EPIC (European Photon Imaging Camera; Strüder et al. 2001; Turner et al. 2001) PN and MOS detectors are produced using the EPCHAIN and EMCHAIN tasks of SAS respectively. High particle background intervals associated with solar flares are filtered out to produce clean event files as well as X-ray images and exposure maps in five energy bands (0.5 – 8, full; 0.5 – 2, soft; 2 – 8, hard; 5 – 8, very hard; 7.5 – 12 keV, ultra-hard). X-ray Sources are independently detected in each of the spectral bands above by applying a Poisson false-detection probability threshold of $P < 4 \times 10^{-6}$. The *XMM* astrometric frame is refined using the EPOSCORR task of SAS and adopting as external astrometric reference the SDSS (Sloan Digital Sky Survey; Gunn et al. 2006) DR8 catalogue (Aihara et al. 2011). The resulting positional accuracy of X-ray sources is about 1''.5 (1 σ rms). The final X-ray source catalogue consists of 8,445 unique sources detected in at least one of the above spectral bands. In this paper we focus on the hard band (2-8 keV) selected sample which has a total of 2768 unique sources.

The sensitivity of the survey is estimated using methods described in Georgakakis et al. (2008) and Georgakakis & Nandra (2011). Figure 1 plots the XMM-XXL-N area curve as a function of EPIC PN count rate. This curve measures the total X-ray survey area that is sensitive to sources of a given count rate in the 2-8 keV (hard) band.

2.2 Optical and near-infrared photometry

Liu et al. (2016) present optical identifications of the X-ray sources in the equatorial field of the XMM-XXL-N survey field with the SDSS-DR8 photometric catalogue (Aihara et al. 2011). In this paper we cross-correlate the X-ray source positions with the deeper optical photometric catalogue (*ugriz* bands; AB limiting magnitude $r \approx 24.9$ mag) of the Canada-France Hawaii Telescope Lensing Survey (CFHTLenS; Heymans et al. 2012; Erben et al. 2013). The association of X-ray sources with counterparts was based on the likelihood ratio method (Sutherland & Saunders 1992; Ciliegi et al. 2003; Brusa et al. 2007; Laird et al. 2009; Luo et al. 2010; Xue et al. 2010; Georgakakis & Nandra 2011).

Potential counterparts are searched for within a radius of 4''.5 from the X-ray centroid, i.e. out to a distance three times the 1 σ X-ray positional rms uncertainty. For each possible identification we measure the likelihood ratio, LR, between the probability that the source, at the given distance from the X-ray position and with the given optical magnitude, is the true counterpart and the probability that the source is a spurious alignment

$$\text{LR} = \frac{q(m)f(r)}{n(m)}, \quad (1)$$

where $q(m)$ represents the magnitude distribution of the true optical counterparts at a given waveband and $f(r)$ is the probability of finding the true counterpart at distance r from the X-ray centroid, given the typical positional uncertainties of the X-ray and optical catalogues. $n(m)$ is the background density of galaxies with magnitude m at a given waveband. For each X-ray/optical source pair the LR is estimated separately in the *ugriz* optical bands of the CFHTLenS. The pair is then assigned the maximum LR of the 5 wavebands.

We approximate $f(r)$ by the normal distribution with standard deviation 1''.5. In this calculation we assume that the positional uncertainty of the optical catalogue is much smaller than that of X-ray sources. The probability $q(m)$ is estimated by subtracting from the magnitude distribution of all possible counterparts of all X-ray sources within a search radius of 4''.5 the expected magnitude distribution of background/foreground galaxies and stars. For the latter, we randomly place 4''.5 radius apertures within the survey area to construct the expected magnitude distribution of optical sources in random sight-lines.

We assess how secure the optical counterpart of an X-ray source is via the reliability parameter defined by Sutherland & Saunders (1992)

$$\text{Rel} = \frac{\text{LR}}{\sum_j \text{LR}_j + (1 - Q)}, \quad (2)$$

where the summation is over all the potential counterparts of the X-ray source within the search radius. Q is the fraction of X-ray sources with identifications to the limiting magnitude of a given CFHTLenS waveband. We define as sample completeness the fraction of X-ray sources with counterparts above a given likelihood threshold, $\text{LR} > \text{LR}_{th}$. Sample reliability is then the mean Rel of the all counterparts with $\text{LR} > \text{LR}_{th}$. We choose the value LR_{th} that maximises the sum of the sample completeness and sample reliability. We adopt $\text{LR}_{th} = 0.4$ and find a total of 4673 CFHTLenS

counterparts out of 5914 XMM-XXL-N X-ray sources that lie within the CFHTLenS footprint ($\approx 80\%$ identification rate), i.e. accounting for the geometry of the optical survey and masked regions associated with bright stars. In the case of the hard-band ($2 - 8$ keV) selected sample, which is the focus of this paper, there are 1778 CFHTLenS counterparts out of 2018 XMM-XXL-N X-ray sources that lie within the CFHTLenS footprint ($\approx 88\%$ identification rate). The expected spurious identification rate is about 5%. In the analysis that follows we use the 2018 XMM-XXL-N X-ray sources that overlap with the CFHTLenS footprint.

For the estimation of photometric redshifts (see below) we complemented the CFHTLenS optical data with far-UV, near-infrared, and mid-infrared photometry available in the XMM-XXL-N field. The positions of the CFHTLenS counterparts are cross-matched within $3''.5$ to GALEX (Galaxy Evolution Explorer) sources using the GALEX All-Sky Imaging Survey Data Release 5 (GALEX-GR5; Bianchi et al. 2011). The probability of a spurious GALEX source within the search radius is about 1.5%. Near-infrared photometry is from public extragalactic surveys that are been carried out by the Visible and Infrared Survey Telescope for Astronomy (VISTA; Emerson 2004), the European Southern Observatory's (ESO) 4-m class telescope dedicated to imaging the southern sky. The VISTA Deep Extragalactic Observations survey (VIDEO; Jarvis et al. 2013) provides photometry in the *ZYJHKs* bands to the depth $Ks(AB) \approx 24$ mag over a total area of 12 deg^2 split in three distinct fields. The VISTA Hemisphere Survey (VHS; PI McMahon, Cambridge, UK) will image the entire southern sky in at least the *J* and *Ks* filters to a limiting magnitude of $Ks(AB) \approx 20$ mag, with certain regions of the survey, like the XMM-XXL-N, also observed in the *H*-band. The data we used are from the 4th Data Release (DR4) of the VIDEO survey and the 3rd Data Release (DR3) of the VHS produced by the Vista Science Archive (VSA), which maintains data products generated by the VISTA InfraRed CAMera (VIRCAM). The VISTA Data Flow System pipeline processing and science archive are described in Irwin et al. (2004), Hambly et al. (2008) and Cross et al. (2012). The VIDEO-DR4 covers about 3.6 deg^2 within the XMM-XXL-N survey field, while the VHS-DR3 covers the entire field. The search radius for cross-matching CFHTLenS positions with VIDEO-DR4 and VHS-DR3 counterparts is fixed to $1''.5$. For 99% of the associations the radial offsets between the optical and near-infrared positions are less than $0''.5$. At the depth of the VIDEO-DR4 survey ($Ks \approx 24$ mag) the probability of a spurious near-infrared galaxy within $0''.5$ is 2%. The AllWISE data are used to compile mid-infrared photometry in the WISE W1, W2, W3, and W4 bands with central wavelengths of 3.4, 4.6, 12, and $22 \mu\text{m}$ respectively. The X-ray/AllWISE identification follows the likelihood ratio method as described in Menzel et al. (2016). Finally, we also cross-match the positions of the optical counterparts of X-ray sources to the SWIRE (Spitzer Wide-area InfraRed Extragalactic) DR2 source catalogue (Surace et al. 2005) using a search radius of $1''.5$. The Spitzer/SWIRE survey covers about 9 deg^2 in the XMM-XXL-N field. The Spitzer photometry is not used in the determination of photometric redshifts but only to explore the positions of X-ray sources on the Spitzer mid-infrared colour-colour diagrams proposed in the literature to select AGN (see section 4). A summary of the multiwavelength

properties of the XMM-XXL-N 2-8 keV selected sample is presented in Table 1.

2.3 Optical spectroscopy

There are a number of spectroscopic surveys in the XMM-XXL-N survey area targeting various classes of extragalactic populations, both galaxies and AGN. A dedicated follow-up spectroscopic programme of X-ray sources in the XMM-XXL-N equatorial field was carried out by the Sloan telescope as part of the SDSS-III ancillary programme (Alam et al. 2015). A detailed description of these data including visual inspection and redshift quality assessment are presented in Menzel et al. (2016). The XXL equatorial field also lies within the footprint of the SDSS-III Baryon Oscillation Spectroscopic Survey (BOSS; Dawson et al. 2013) programme, which provides redshifts for UV/optically-selected broad-line QSOs and luminous red galaxies. Stalin et al. (2010) presents redshifts for X-ray sources in the original XMM-LSS survey field (Clerc et al. 2014), which is part of the larger XMM-XXL survey. The VIMOS Public Extragalactic Redshift Survey (VIPERS, Garilli et al. 2014; Guzzo et al. 2014) targets galaxies to a magnitude limit of $i(AB) = 22.5$ mag, which are pre-selected on the basis of their optical colours to maximise the number of spectroscopic identifications in the redshift interval $z = 0.5 - 1.2$. The first public data release of the VIPERS includes a total of 30,523 sources in the equatorial XMM-XXL-N field and covers about 5 deg^2 of the X-ray survey area. The VIMOS VLT Deep Survey (VVDS; Le Fèvre et al. 2013) provides spectroscopy for about 10000 optically-selected sources to $i(AB) = 24$ mag over an area of about 0.5 deg^2 within the XXL equatorial field. The ESO large programme 180.A-0776 (P.I. O. Almaini) followed with spectroscopy about 3000 galaxies to $K(AB) = 23$ mag selected in the UKIDSS Ultra-deep Survey Field (UDS). A description of these observations is presented in Bradshaw et al. (2013) and McLure et al. (2013).

The spectroscopic catalogues are matched to the CFHTLenS optical positions within a radius of 1 arcsec. We select redshifts with quality flags in the published catalogues from which they were retrieved that indicate a probability better than $\approx 90\%$ of being correct. There are 2311 redshift measurements out of 4673 X-ray sources with CFHTLenS identifications. The majority (2012) are from the SDSS spectroscopic programmes. There are a further 129 redshifts from Stalin et al. (2010), 91 from the UDS follow-up spectroscopy, 62 from VIPERS and 17 from VVDS. The number of spectroscopic identifications of the XMM-XXL-N 2-8 keV selected sample is listed in Table 1 and their breakdown to optically resolved and unresolved sources is shown in Table 2.

2.4 Photometric redshifts

For X-ray sources without optical spectroscopy we estimate photometric redshifts using the LEPHARE code (Photometric Analysis for Redshift Estimate; Arnouts et al. 1999; Ilbert et al. 2006). We apply different cuts to the X-ray selected sample to optimise the template fits to the observed Spectral Energy Distributions (SEDs) of certain groups of

Table 1. Hard-band (2-8 keV) selected sample of the XMM-XXL-N survey

Total number of X-ray sources (1)	X-ray sources within CFHTLenS (2)	Number of CFHTLenS IDs (3)	VIDEO photometry (4)	AllWISE photometry (5)	GALEX photometry (6)	<i>Spitzer</i> photometry (7)	spectroscopic redshifts (8)
2768	2018	1778	605	1503	473	944	936

(1) Total number of X-ray sources detected in the 2-8 keV (hard) energy band in the XMM-XXL-N sample. (2) Number of 2-8 keV detected XMM-XXL-N sources that lie within the good photometry area of the CFHTLenS survey (Heymans et al. 2012; Erben et al. 2013). (3) Number of hard-band detected X-ray sources with optical associations in the CFHTLenS survey. (4) Number of XMM-XXL-N 2-8 keV detected X-ray sources with CFHTLenS counterparts that lie within the VIDEO-DR4 survey area. (5) Number of XMM-XXL-N 2-8 keV detected X-ray sources with CFHTLenS identifications and AllWISE counterparts. (6) Number of XMM-XXL-N 2-8 keV detected X-ray sources with CFHTLenS identifications and GALEX-GR5 (Bianchi et al. 2011) associations. (7) Number of XMM-XXL-N 2-8 keV detected X-ray sources with CFHTLenS identifications and *Spitzer*/SWIRE-DR2 (Surace et al. 2005) counterparts. (8) Number of XMM-XXL-N 2-8 keV detected X-ray sources with CFHTLenS identifications and spectroscopic redshift measurements.

Table 2. Summary of redshift measurements for the hard-band (2-8 keV) selected sample of the XMM-XXL-N survey

sample (1)	optically unresolved (2)	optically resolved	
		CFHTLenS (3)	VIDEO (4)
spec-zs	580	264	92
photo-zs	331	367	144

(1) Photometric or spectroscopic redshift subsample of the 2-8 keV (hard) selected XMM-XXL-N sources. (2) X-ray sources with unresolved optical light profile (point-like). Sources in that sample without spectroscopy are assigned photometric redshift probability density functions derived from the dN/dz of spectroscopically confirmed sources (see text for details). (3) X-ray sources with resolved optical light profile and without available deep near-infrared photometry from the VIDEO survey. (4) X-ray sources with resolved optical light profile and available deep near-infrared photometry from the VIDEO survey.

sources, and improve the overall quality of the photometric redshift estimates. We present results separately for X-ray sources that overlap with the VIDEO survey area and therefore benefit from the deep near-infrared photometry of that programme. Different template libraries are applied to X-ray sources associated with optically resolved (extended optical light profile) and unresolved (point-like) counterparts. This is motivated by the work of Salvato et al. (2009) who found that the morphological information of the optical counterparts of X-ray sources can be used as a prior when computing photometric redshifts. X-ray AGN associated with optically extended sources are typically at low and moderate redshifts and have SEDs with a large contribution from the host galaxy. Point-like sources have SEDs dominated by emission from the central engine and are likely to lie, on average, at higher redshifts. In addition to the different template library for each morphological class, we follow Salvato et al. (2009) and impose a B -band absolute magnitude prior $-30 < M_B < -20$ mag when estimating the photometric redshifts of the optically unresolved sample. X-ray sources with stellerity parameter in the publicly available CFHTLenS catalogues $CLASS_STAR > 0.8$ are considered optically unresolved, and are likely to be dominated by emission from the AGN in the optical bands. It is also found that using different templates for samples split by X-ray flux also

improves the photometric redshift results. Previous studies have shown that the template libraries used to determine photometric redshifts for X-ray selected AGN in bright surveys (e.g. XMM-COSMOS Salvato et al. 2009) cannot be applied to sources detected at fainter flux limits in deeper samples, such as the 4 Ms Chandra Deep Field South (Hsu et al. 2014).

The model template libraries that are applied independently to different sub-samples of X-ray sources are (i) the galaxy SEDs of Ilbert et al. (2009), (ii) the hybrid QSO/galaxy templates presented by Salvato et al. (2011) and (iii) the templates developed by Tasnim Ananna et al. (in prep.) for the determination of photometric redshifts for X-ray sources in the Stripe82X survey field (LaMassa et al. 2016). Extinction is added to the templates as a free parameter using the Calzetti et al. (2000) and the Prevot et al. (1984) attenuation laws. The photometry used for X-ray sources in different wavebands corresponds to the ‘total’ source flux estimates in the corresponding catalogue. For the VIDEO and the VHS surveys in particular we use either Kron or Petrosian-type magnitudes (appropriate for resolved sources), or fluxes integrated within fixed-size apertures (corrected for losses because of the size of the Point Spread Function), which are listed in the VSA databases. Before estimating photometric redshifts we explore potential systematic offsets among photometric bands, which may arise because of e.g. variations in seeing conditions as a function of observing time and wavelength, differences in the definition of ‘total’ magnitude in different catalogues. Such zero-point offsets among wavebands are estimated by LEPHARE using a total of 2463 spectroscopically confirmed galaxies from the VIPERS-DR1 (Garilli et al. 2014; Guzzo et al. 2014). The redshift is fixed and the best-fit template for each source is found. Photometric offsets are then estimated for each waveband to minimize the differences between the model templates and the observed magnitudes. These offsets are then applied to the observed photometry prior to the determination of photometric redshifts. Spectroscopically confirmed X-ray selected AGN are not the optimal sample for this calculation because of potential variability issues affecting different photometric bands observed at separate epochs.

In the case of optically-unresolved X-ray sources ($CLASS_STAR > 0.8$) we use the hybrid QSO/galaxy template library of Salvato et al. (2011) for X-ray fluxes $f_X > 10^{-13}$ erg s $^{-1}$ cm $^{-2}$, and the templates of Tasnim Ananna

et al. (in prep.) for fainter X-ray sources. The quality¹ of the photometric redshift measurements is rather poor with $\sigma_{NMAD} = 0.07$ and outlier fraction $\eta = 27\%$. These numbers do not improve for sources with near-infrared information from the VIDEO or VHS surveys. Salvato et al. (2011) showed that for broad-line X-ray selected QSOs with blue featureless continua, narrow-band photometry as well as some handle on the source variability are essential to reduce η below the 10% level. Without this additional information and for the spectral bands used in this work, Salvato et al. (2011) estimate an expected catastrophic failure redshift rate of $\eta \approx 20 - 40\%$, similar to what is found here. Another potential issue relates to the separation between optically extended and point-like sources using morphological information from seeing-limited ground-based images. Hsu et al. (2014) for example, underlined the importance of high spatial resolution imaging from e.g. the Hubble Space Telescope to identify optically unresolved X-ray sources and apply the correct set of templates to the different morphological classes. The poor quality of the photometric redshift estimates for optically unresolved X-ray sources is mirrored by the corresponding photometric redshift Probability Distribution Functions (PDZs), which are typically broad. It is found for example, that for the majority (89%) of the optically unresolved X-ray AGN with available spectroscopy, the true redshift (i.e. spectroscopic) lies within the 5th and 95th percentiles of the estimated PDZ distribution. We wish to propagate the uncertainties in the photometric redshift estimates of point-like X-ray AGN in the analysis. There are at least two ways to achieve that. The first is to use directly the PDZs of individual sources. The second exploits the fact that most of the optically unresolved XMM-XXL-N X-ray sources have spectroscopic redshift measurements (e.g. 580 out of 911 in the hard-band selected sub-sample; see Table 2), and therefore the redshift distribution of the population is well constrained (see Fig. 2). We may therefore assume that optically unresolved X-ray sources without spectroscopic redshifts follow the same redshift distribution, $dN(z)/dz$, as the spectroscopically confirmed part of the population in the XMM-XXL-N field. This latter approach is adopted in the analysis that follows. We note however, that our results on the AGN space density (Section 4) do not change if instead we adopt the PDZs of individual sources. This is because the broad PDZs produced by LEPHARE are representative of the overall level of uncertainty in the determination of photometric redshifts for X-ray sources with point-like optical profiles.

Figure 2 plots the spectroscopic redshift histogram of X-ray AGN that are unresolved in the optical bands. This distribution is fit with the function $dN(z)/dz \propto \exp[-(z - \bar{z})^2/2\sigma_z^2]$, where \bar{z} and σ_z are free parameters (red curve in Figure 2). Spectroscopically unidentified and optically unresolved X-ray sources are assigned a redshift PDZ that follows the relation above. We caution that the optically unresolved X-ray sources without spectroscopic redshifts extend to fainter optical magnitudes (median $r \approx 22$ mag) compared to the spectroscopically confirmed part of the pop-

ulation (median ≈ 20.5 mag). Nevertheless, we find that the redshift distribution of the optically unresolved X-ray sources with secure redshifts is not a strong function of magnitude. The median and 68th percentiles of the distribution increase from $z = 1.4_{-0.6}^{+0.8}$ for sources with $r < 21.5$ mag to $z = 1.7_{-0.7}^{+0.6}$ for $r > 22$ mag. These numbers are broadly confirmed using the recent COSMOS-Legacy X-ray source catalogue (Marchesi et al. 2016). We select a total of about 100 X-ray sources from that sample with relatively bright X-ray fluxes $f_X(2 - 10 \text{ keV}) > 10^{-14} \text{ erg s}^{-1} \text{ cm}^{-2}$ similar to the XMM-XXL-N limit, optically faint counterparts $r > 22.0$ mag and unresolved optical light profiles. The redshift (photometric or spectroscopic) distribution of this subset has a median and 68th percentiles $z = 1.5_{-0.3}^{+0.4}$.

X-ray sources with extended optical profiles (CFHTLenS parameter CLASS_STAR < 0.8) are likely to have broad-band optical/near-infrared emission dominated by stellar light with little contamination from the central engine. For these sources normal galaxy templates may provide an adequate representation of the broad-band SEDs. Experimentation showed that the best photometric redshift results for this class of sources are obtained by adopting the Ilbert et al. (2006) normal galaxy template library for sources with X-ray fluxes $f_X < 10^{-14} \text{ erg s}^{-1} \text{ cm}^{-2}$ and the hybrid QSO/galaxy templates developed by Tasnim Ananna et al. (in prep.) for brighter sources. For optically extended X-ray sources with additional near-infrared photometry from the VIDEO survey we estimate photometric redshift quality measures $\sigma_{NMAD} = 0.06$ and $\eta = 4.5\%$. Figure 3 explores further the quality of the photometric redshifts for X-ray AGN by plotting the quantity $(z_{phot} - z_{spec})/(1 + z_{spec})$ as a function of spectroscopic redshift and r -band optical magnitude. The catastrophic redshift failure rate does not appear to change with optical magnitude, at least to the limit $r \approx 23$ mag, where sufficient numbers of spectroscopically confirmed sources is available. The fraction of catastrophic redshift failures also appears to be stable with redshift at least out to $z \approx 1$. In the analysis that follows optically extended X-ray sources with VIDEO near-infrared photometry are assigned the PDZs determined directly by the LEPHARE code.

The availability of deep infrared photometry in addition to optical data is key for good quality photometric redshift measurements in the case of optically extended X-ray sources. For the subset of this population that lies outside the VIDEO near-infrared survey area we estimate photometric redshift quality measures $\sigma_{NMAD} = 0.06$ and $\eta = 16\%$. The VHS survey near-infrared photometry, which is available over the entire XMM-XXL-N field, is shallower ($K_s \approx 20$ mag) than the VIDEO survey ($K_s \approx 24$ mag), and does not substantially improve the photometric redshifts of optically-extended X-ray sources. Also, the relatively high catastrophic redshift fraction is not represented in the broadness of the PDZs estimated by the LEPHARE. Only about half of the optically extended X-ray sources outside the VIDEO area with available optical spectroscopy have PDZs with 5th and 95th percentiles that bracket the true spectroscopic redshift. Therefore for this class of sources we choose a different approach for propagating the photometric redshift uncertainties in the analysis that follows. Figure 4 shows the distribution of the quantity $|z_{phot} - z_{spec}|/(1 + z_{spec})$ for the sample of spectroscopically confirmed and optically

¹ The quality of photometric redshifts is quantified by the rms scatter, σ_{NMAD} , of the quantity $|z_{spec} - z_{phot}|/(1 + z_{spec})$ and the outlier fraction, η , defined as $\eta = |z_{spec} - z_{phot}|/(1 + z_{spec}) > 0.15$.

extended XMM-XXL-N X-ray sources outside the VIDEO area, where the parameters z_{phot} , z_{spec} in the relation above are the photometric and the spectroscopic-redshift measurements, respectively. The distribution of this quantity can be represented with a Lorentzian that has wings which are sufficiently broad and consistent with the estimated catastrophic redshift fraction, $\eta = 16\%$. In the analysis that follows uncertainties and potential systematics affecting photometric redshift measurements for optically extended X-ray selected AGN without VIDEO photometry are compensated for, at least to the first approximation, by using PDZs derived from the Lorentzian plotted in Figure 4.

In Figure 5 we explore further the quality of the photometric redshift estimates for optically extended light profile and without VIDEO photometry. There is no strong trend of increasing η at faint optical magnitudes, although the number of spectroscopically confirmed X-ray AGN beyond $r \approx 22.5$ mag drops substantially and therefore small number statistics affect any conclusions. The fraction of catastrophic redshift failures in Figure 5 appears to increase at redshifts $z \gtrsim 1$. We note however the small number of spectroscopic redshift measurements of X-ray sources with extended optical light profile beyond $z = 1$, which has an impact on any conclusions.

In addition to optically identified X-ray sources in the sample there are also 240 2-8 keV detections in the XMM-XXL-N without secure counterparts in the CFHTLenS (12% of the sample; see Table 1). Figure 6 presents the X-ray flux distribution of these sources. The majority have $f_X(2 - 10 \text{ keV}) > 10^{-14} \text{ erg s}^{-1} \text{ cm}^{-2}$. We explore the expected redshift distribution of this population using the 2 deg²-wide COSMOS-Legacy survey (Civano et al. 2016; Marchesi et al. 2016). We select COSMOS-Legacy survey X-ray sources with $f_X(2 - 10 \text{ keV}) > 10^{-14} \text{ erg s}^{-1} \text{ cm}^{-2}$ and faint optical counterparts, $r > 24.5$ mag, i.e. close to limiting magnitude of the CFHTLenS survey data used in this paper. We use spectroscopic or photometric redshifts for these sources listed in Marchesi et al. (2016). The resulting redshift distribution is shown in Figure 7. Most sources are in the interval at $z = 1 - 3$. We choose to assign XMM-XXL-N sources without optical counterparts a weak prior that is flat in the redshift interval $z = 1 - 6$. The breakdown of redshift measurements, photometric or spectroscopic, for the 2-8 keV selected XMM-XXL-N sample are presented in Table 2.

2.5 X-ray spectral analysis

The X-ray spectra of individual sources are extracted following methods described in Liu et al. (2016). Events with patterns up to 4 and 12 for the PN and MOS detectors, respectively, are included. The relevant ARF and RMF calibration files are generated using the SAS tasks ARFGEN and RMFGEN. Because of the similar responses of the MOS1 and MOS2 CCDs, the spectra from those two detectors are coadded into a single spectrum.

The Bayesian X-ray Analysis package (BXA; Buchner et al. 2014, 2015) is used to fit the X-ray spectra of individual sources. The adopted model includes (i) components that account for photoelectric absorption and Compton scattering from obscuring material along the line-of-sight that is distributed with a toroidal geometry close to the central supermassive black hole, (ii) an independent soft compo-

nent, which is often observed in the spectra of obscured AGN (e.g. Brightman & Nandra 2012; LaMassa et al. 2012, 2014; Buchner et al. 2015; Lanzuisi et al. 2015) and could be attributed to Thomson scattering of the intrinsic X-ray emission off ionised material within the torus opening angle (e.g. Guainazzi & Bianchi 2007), (iii) Compton scattering (reflection) of radiation on dense material outside the light-of-sight. We adopt the torus model of Brightman & Nandra (2011a) to approximate the transmitted spectrum of an AGN through obscuring material. The intrinsic spectrum is assumed to follow a power-law parametrised by the spectral index Γ . The Brightman & Nandra (2011a) model assumes a sphere of constant density with two symmetric conical wedges with vertices at the centre of the sphere removed. The opening angle of the cones is fixed to 45° and the viewing angle of the observer is set to the maximum allowed in the model, 87°, i.e. nearly edge on. The soft component is approximated by a power-law model with the same spectral index, Γ , as the intrinsic power-law spectrum. The reflection component is modelled with the PEXRAV model presented by Magdziarz & Zdziarski (1995). The spectral index of that component is the same as that of the intrinsic power-law spectrum.

The adopted model (TORUS + ZPOWERLW + PEXRAV in XSPEC terminology) has five free parameters, the slope of the intrinsic power-law spectrum, Γ , the line-of-sight column density of the obscurer, N_H , the normalisations of the intrinsic power-law, soft scattering and reflection components. The adopted spectral model is a trade-off between a reasonable representation of the basic AGN X-ray spectral components found in local samples and a relatively small number of free parameters to be constrained from data with typically low number of photons. Buchner et al. (2014) also showed that the adopted spectral components are the minimum needed to represent the X-ray properties of AGN in the *Chandra* Deep Field South. We impose that the normalisations of the soft power-law and reflection components cannot exceed 10% of the intrinsic power-law spectrum. The redshift of the soft power-law and reflection component is tied to that of the torus model. We use a Gaussian prior for the spectral index Γ with mean 1.95 and standard deviation 0.15 (Nandra & Pounds 1994). The hydrogen column density of the line-of-sight obscuration is assigned a flat prior in the logarithmic range $\log_{10}(N_H/\text{cm}^{-2}) = 20 - 25$. The source redshift is fixed to the spectroscopic value if available. In the case of photometric redshift estimates the corresponding PDZs are used as priors. The XMM PN and MOS background spectrum is fit with the models constructed by Maggi et al. (2014) that include an empirical instrumental component (Sturm 2012) and an astrophysical component (Kuntz & Snowden 2010). The energy range used in the spectral analysis is 0.5 – 8 keV. The output of the spectral analysis using the BXA are posterior probability distribution functions in the multidimensional space of the spectral fit free parameters. These are then converted to posterior chains in the parameter space of intrinsic AGN luminosity [$\log L_X(2 - 10 \text{ keV})$], hydrogen column density ($\log N_H$) and redshift (z).

Figure 8 plots the distribution of total (source and background) spectral counts in the 0.5-8 keV band of the XMM-XXL-N X-ray sources. The median of this distribution is 63 photons. For completeness also shown in Figure 8 is the

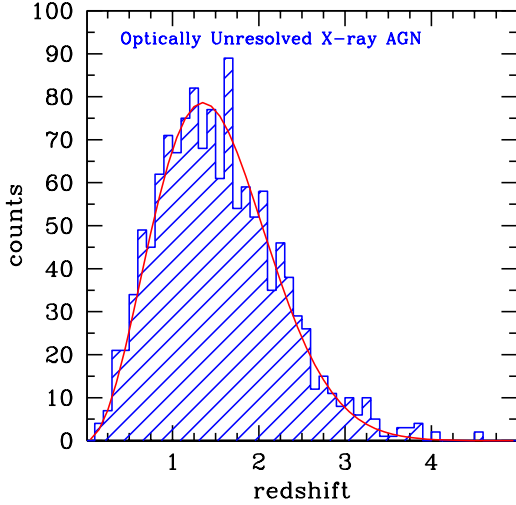


Figure 2. Spectroscopic redshift distribution of X-ray selected AGN in the XMM-XXL-N field with unresolved optical light profiles (point-like). The red curve is the best-fit function of the form $dN(z)/dz \propto \exp[-(z - \bar{z})^2/2\sigma_z^2]$, where \bar{z} and σ_z are free parameters.

source only (i.e. after subtracting the expected background counts) spectral count histogram. We note however, that when analysing the X-ray spectra of individual sources the background is not subtracted but fitted to the data as a separate model component. The uncertainties of the derived parameters (e.g. $\log N_H$) depend on the energy distribution of the photons (i.e. overall spectral shape) and on the accuracy of the adopted redshift measurements (i.e. spectroscopic vs photometric). Examples of confidence intervals for the $\log N_H$ and $\log L_X$ of individual sources with spectroscopic redshift measurements are presented in Figures 11 and 12 of Section 4.

Figure 9 presents the distribution on the intrinsic X-ray luminosity (i.e. corrected for line-of-sight obscuration) vs redshift space of the XMM-XXL-N X-ray sources in comparison with the Chandra surveys in the COSMOS (Elvis et al. 2009), Extended Growth Strip (AEGIS-XD Nandra et al. 2015) and 4 Ms Chandra Deep Field South (Xue et al. 2011; Rangel et al. 2013). For the Chandra survey fields the data-points are based on the spectral analysis results of Buchner et al. (2015). This figure demonstrates the complementarity of the XMM-XXL-N sample to Chandra survey fields.

3 X-RAY LUMINOSITY FUNCTION DETERMINATION

This section describes our methodology for determining the X-ray luminosity function of AGN. This is defined as the space density of the population at a given redshift (z), X-ray accretion luminosity in the 2-10 keV energy band [$L_X(2 - 10 \text{ keV})$], and obscuration along the line-of-sight parametrised by the column density of neutral hydrogen (N_H). The likelihood of a particular luminosity function parametrisation given a set of observations is described

by the product of the Poisson probabilities of individual sources.

$$\mathcal{L}(d_i | \theta) = e^{-\lambda} \times \prod_{i=1}^N \int d \log L_X \frac{dV}{dz} dz d \log N_H \times p(d_i | L_X, z, N_H) \phi(L_X, z, N_H | \theta), \quad (3)$$

where dV/dz is the comoving volume per solid angle at redshift z , d_i signifies the data available for source i and θ represents the parameters of the luminosity function model, $\phi(L_X, z, N_H | \theta)$, that are to be determined. The multiplication is over all sources, N , in the sample and the integration is over redshift, X-ray luminosity and hydrogen column density. The quantity $p(d_i | L_X, z, N_H)$ is the probability of a particular source having redshift z , X-ray luminosity L_X and line-of-sight hydrogen column density N_H . This captures uncertainties in the determination of all three parameters because of e.g. photometric redshift errors or uncertainties in the X-ray spectra, under the assumption that the adopted spectral model provides a reasonable representation of the basic AGN X-ray spectral properties (e.g. see Buchner et al. 2014). In equation 3, λ is the expected number of detected sources in a survey for a particular set of model parameters θ

$$\lambda = \int d \log L_X \frac{dV}{dz} dz d \log N_H \times A(L_X, z, N_H) \phi(L_X, z, N_H | \theta). \quad (4)$$

where, $A(L_X, z, N_H)$ is the sensitivity curve, which quantifies the survey area over which a source with X-ray luminosity L_X , redshift z and column density N_H can be detected. A non-parametric approach for the determination of the AGN space density is adopted. A three-dimensional grid in redshift, luminosity and column density is defined and $\phi(L_X, z, N_H)$ is assumed to be constant within each cube pixel with dimensions $(\log L_X \pm d \log L_X, z \pm dz, \log N_H \pm d \log N_H)$. The value of the AGN space density in each grid pixel is determined via equation 3. The edges of the grid pixels in each of the three dimensions are $\log L_X = (41.0, 42.0, 42.5, 43.0, 43.5, 44.0, 45.0, 46.0, 47.0)$, $z = (0.0, 0.5, 1.0, 1.5, 2.0, 6.0)$, $\log N_H = (20.0, 22.0, 23.0, 24.0, 25.0)$. The total number of free model parameters is 160.

Importance sampling (Press et al. 1992) is used to evaluate the integrals in equation 3. For each source we draw $(\log L_X, z, \log N_H)$ points from the equal probability chains produced by the X-ray spectral analysis step. The luminosity function is then evaluated for each sample point, (L_X, z, N_H) . The integral of equation 3 is simply the average luminosity function of the sample. The Hamiltonian Markov Chain Monte Carlo code Stan² (Carpenter et al. 2016) is used for Bayesian statistical inference.

Finally we define the quantity N_{obs} , the observed number of sources within in each bin of the 3-dimensional grid

² <http://mc-stan.org/shop/>

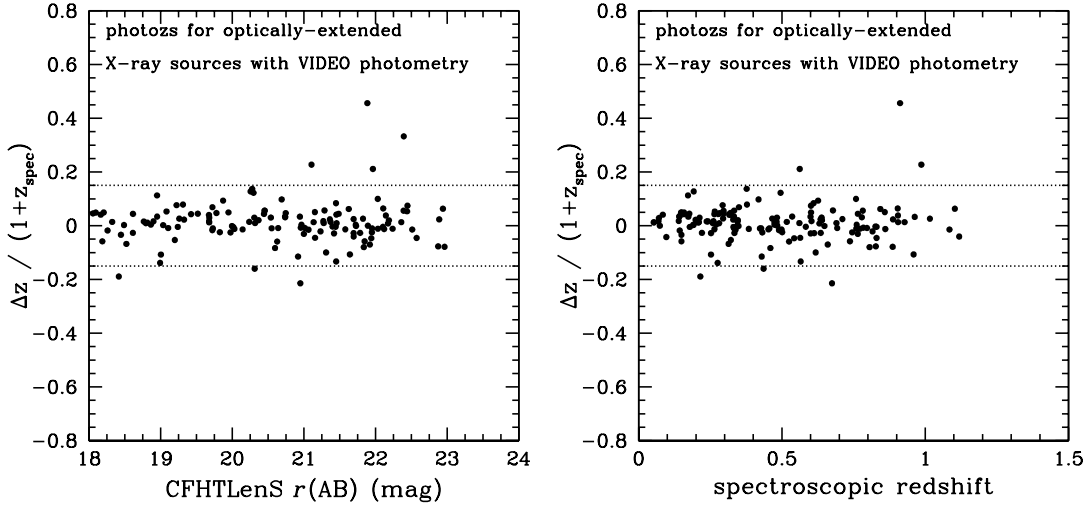


Figure 3. The quantity $(z_{phot} - z_{spec})/(1 + z_{spec})$ is plotted as a function of CFHTLenS r -band magnitude (left panel) and spectroscopic redshift (right panel) for spectroscopically confirmed XMM-XXL-N AGN with extended optical light profiles that lie within the VIDEO-DR4 area. The horizontal dotted lines mark the catastrophic failure limit, $\eta > 0.15$.

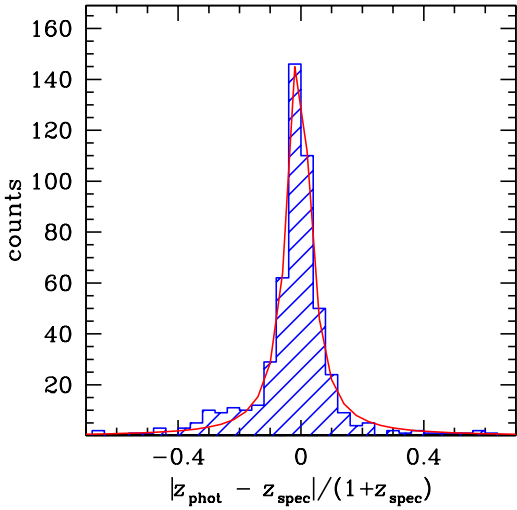


Figure 4. Histogram of the quantity $(z_{phot} - z_{spec})/(1 + z_{spec})$ for XMM-XXL-N X-ray sources that (i) lie outside the footprint of the VIDEO-DR4 deep near-infrared survey, (ii) have counterparts with extended optical light profiles and (iii) have spectroscopic redshift measurements. The red curve is the best-fit Lorentzian distribution to the observed histogram. The broad wings of that distribution provide a reasonable representation of the overall uncertainty of the photometric redshifts, including catastrophic failures.

in redshift, luminosity and column density (see also Miyaji et al. 2001; Aird et al. 2015a)

$$N_{obs} = \sum_{i=1}^N \frac{1}{N_i} \int d \log L_X \frac{dV}{dz} dz d \log N_H \times p(d_i | L_X, z, N_H) \phi(L_X, z, N_H | \theta), \quad (5)$$

where the integration limits correspond to the edges of each grid pixel defined above. The summation is over all sources in the sample. The normalisation factor N_i is the integral of the quantity $p(d_i | L_X, z, N_H) \phi(L_X, z, N_H | \theta)$ over the full range of luminosities, redshifts and column densities. N_{obs} is used for the visualisation of the results. Only bins with $N_{obs} > 1$ are shown in the relevant figures and tables. Bins with $N_{obs} < 1$ typically have large errors and therefore the observational constraints on the space density of AGN are loose.

4 RESULTS

4.1 X-ray AGN obscuration distribution

A key aim of this work is to estimate the fraction of obscured AGN at the relatively bright X-ray luminosities sampled by the wide-area and shallow XMM-XXL-N survey. This sample includes a non-negligible fraction of AGN with hydrogen column densities in excess of $N_H = 10^{22} \text{ cm}^{-2}$. This is shown in Figure 10 (left panel), which plots the observed $\log N_H$ histogram of the full XMM-XXL-N hard-band selected sample. We construct this distribution using two different approaches. The first is summing up the posterior probability distribution functions of individual sources produced by the X-ray spectral analysis. This method however, does not take into account the form of the AGN X-ray luminosity function, i.e. the fact that luminous sources are rarer than moderate luminosity ones. We therefore use equation 5 to estimate the observed number of sources, N_{obs} , as a function of the hydrogen column density. This calculation weighs the N_H posterior distribution of individual sources with the value of the corresponding luminosity function. The histogram of the quantity N_{obs} provides a more representative view of the observed N_H distribution of the AGN population detected in the XMM-XXL-N. The fraction of observed sources with column densities $N_H > 10^{22} \text{ cm}^{-2}$ is about 35%. Compton-

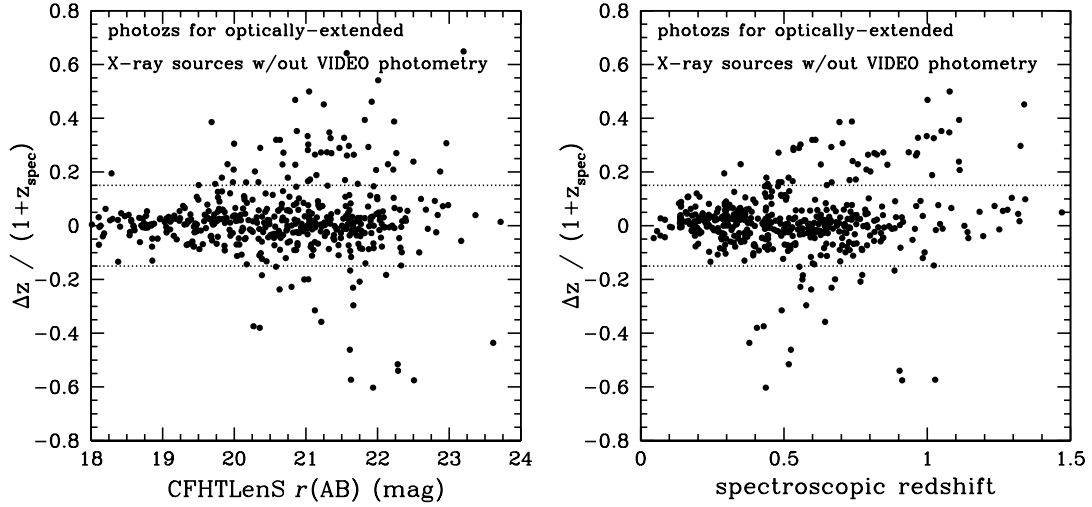


Figure 5. The quantity $(z_{phot} - z_{spec})/(1 + z_{spec})$ is plotted as a function of CFHTLenS r -band magnitude (left panel) and spectroscopic redshift (right panel) for spectroscopically confirmed XMM-XXL-N AGN with extended optical light profiles that lie outside the VIDEO-DR4 footprint. The horizontal dotted lines mark the catastrophic failure limit, $\eta > 0.15$.

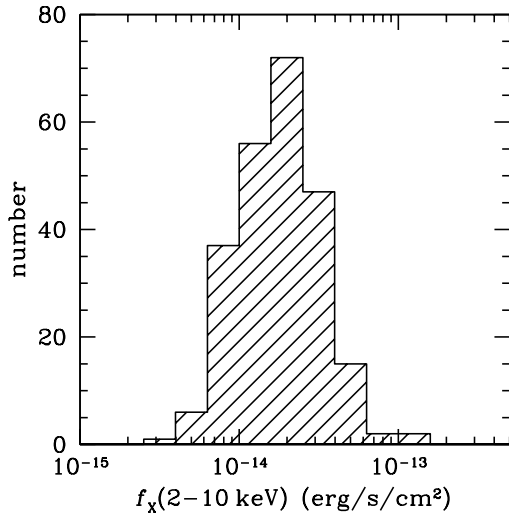


Figure 6. 2-10 keV X-ray flux distribution of XMM-XXL-N sources detected in the 2-8 keV spectral band without secure optical counterparts in the CFHTLenS.

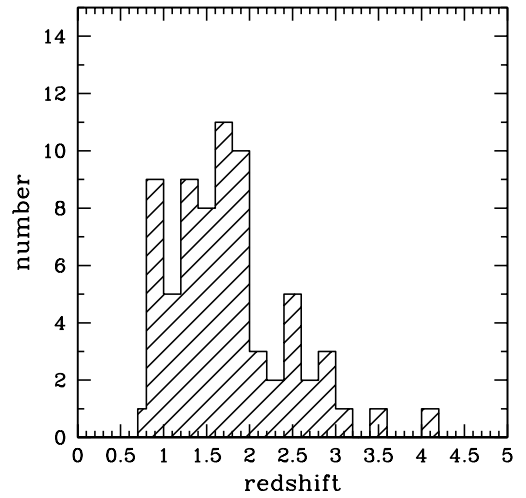


Figure 7. Redshift distribution of X-ray bright, $f_X(2-10 \text{ keV}) > 10^{-14} \text{ erg s}^{-1} \text{ cm}^{-2}$, and optically-faint, $r > 24.5 \text{ mag}$, X-ray sources in the COSMOS Legacy survey (Civano et al. 2016; Marchesi et al. 2016). The redshifts are either spectroscopic or photometric from Marchesi et al. (2016).

thick AGN with $N_H > 10^{24} \text{ cm}^{-2}$ represent a small fraction, $\approx 2\%$, of the observed population in the XMM-XXL field. Figure 10 also shows the $\log N_H$ distribution of the sample split into AGN with optically unresolved (middle panel) and optically-extended (right panel) counterparts. As expected X-ray sources with unresolved (point-like) counterparts are mostly associated with low hydrogen column densities, $N_H > 10^{22} \text{ cm}^{-2}$. AGN identified with optically-resolved galaxies have a flatter $\log N_H$ distribution. Selected examples of individual XMM-XXL-N obscured AGN are also presented in Figure 11. The SDSS optical spectra in this figure show narrow optical emission lines (e.g. [OII] 3727 Å, H β , [OIII] 5007 Å) and/or absorption features (e.g. H+K break,

Balmer lines) associated with the AGN host galaxy. The corresponding posterior probability distributions in accretion luminosity and hydrogen column density inferred from the X-ray spectral analysis are also shown in Figure 11.

Within the XMM-XXL-N sample there are also broad optical emission-line AGN (type-1) that show evidence for X-ray obscuration, $N_H \gtrsim 10^{22} \text{ cm}^{-2}$. Such sources represent about 10% of the type-1 AGN sample in the XMM-XXL-N survey (see Figure 9 of Liu et al. 2016). Examples of this class of AGN are shown in Figure 12. The X-ray obscuration in these systems may be associated with dust-free material

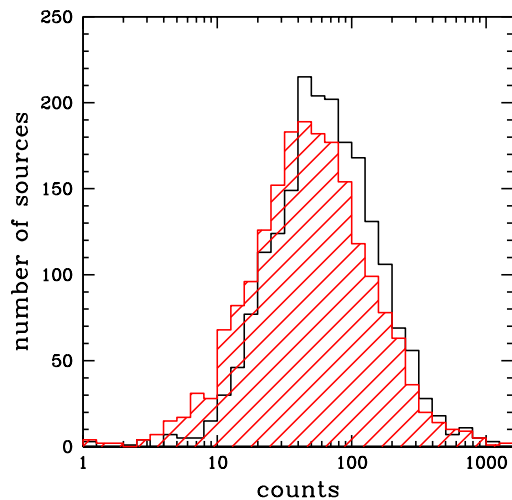


Figure 8. Distribution of spectral photon counts in the 0.5–8 keV energy range of XMM-XXL-N sources. The open black histogram shows the total spectral counts, i.e. source and background, the hatched red histogram corresponds to the source-only counts, i.e. after subtracting for each source the mean expected background contribution.

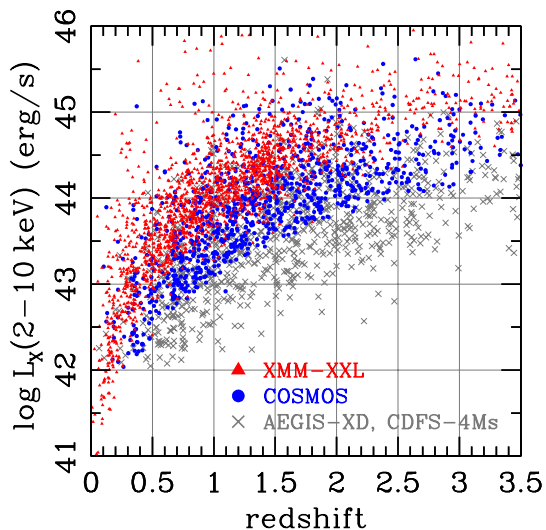


Figure 9. Intrinsic X-ray luminosity (i.e. corrected for line-of-sight obscuration) against redshift for AGN detected in different X-ray surveys. The red triangles correspond to the XMM-XXL-N sample used in this work. The blue circles are X-ray sources detected in the Chandra COSMOS survey (Elvis et al. 2009) and the grey crosses are X-ray selected AGN in the deep Chandra surveys of the Extended Growth Strip (AEGIS-XD; Nandra et al. 2015) and the 4Ms Chandra Deep Field South (CDFS-4Ms; Rangel et al. 2013) fields. The X-ray luminosities for the Chandra survey datapoints are from Buchner et al. (2015) and are estimated from X-ray spectra analysis. Each data point is randomly drawn from the 3-dimensional X-ray luminosity, column density and redshift probability distribution function of individual sources inferred from the X-ray spectral fits.

close to the central black hole and within the broad-line region (Liu et al. 2016).

Figure 13 and Table 3 present the space density of AGN as a function of 2–10 keV X-ray luminosity for the different redshift and hydrogen column density intervals defined in section 3. Results are shown only up to the redshift bin $z = 1.0 - 1.5$. At higher redshifts the XMM-XXL-N space density constraints suffer large uncertainties because of small number statistics, increasing photometric redshift uncertainties and the fraction of optically unidentified sources in the sample, which are expected to be associated preferentially with moderate- and high-redshift AGN. Further observations are needed to mitigate these issues. Deep near-infrared photometry (e.g. VIDEO survey depths) over the full XMM-XXL-N field for example, will allow both identifications and improved photometric redshift estimates for obscured and high redshift AGN at $z \gtrsim 1.5$. Dedicated follow-up spectroscopic surveys of optically faint (e.g. $r \gtrsim 22.5$ mag) X-ray sources in the XMM-XXL-N are also needed to improve constraints on the AGN space density, particularly for obscured sources, at moderate and high redshift. In Figure 13 the non-parametric constraints from the XMM-XXL-N field are also compared with previous estimates of the X-ray luminosity function of AGN (Ueda et al. 2014; Buchner et al. 2015). Overall there is good agreement with previous studies. For Compton-thin AGN in particular, the shallow XMM-XXL-N survey provides competitive constraints on the AGN space density to $L_X(2 - 10 \text{ keV}) \approx 10^{45} \text{ erg s}^{-1}$, i.e. close to and above the knee of the X-ray luminosity function. For Compton-thick levels of obscuration ($N_H > 10^{24} \text{ cm}^{-2}$) we find AGN space densities consistent with the recent work of Buchner et al. (2015). This is also broadly consistent with Ajello et al. (2012) in the case of low redshift Compton-thick AGN selected in the 60-month BAT (Burst Alert Telescope Barthelmy et al. 2005) all sky survey. Also shown are the recent constraints from Akylas et al. (2016) on the luminosity function of Compton-thick AGN using the 70-month Swift-BAT all-sky survey hard X-ray catalogue. The Akylas et al. (2016) space densities are lower than previous studies, including those from Ajello et al. (2012). This discrepancy is surprising given that the two studies find very similar observed fractions of Compton thick sources among the total AGN sample. The source of the difference is likely related to the X-ray spectral models adopted to determine the intrinsic luminosity of heavily obscured sources and the method used to extrapolate from the observed number of Compton-thick sources to the parent population. Our constraints are also systematically higher than those of Ueda et al. (2014). Current estimates of the space density of Compton thick AGN will improve by adding high energy observations, $> 10 \text{ keV}$ (e.g. *NuSTAR*), to the existing X-ray spectroscopy at observed energies below about 10 keV provided by *XMM* or *Chandra*.

We also explore the fraction of obscured Compton-thin AGN as a function of luminosity and redshift. We define this fraction as the ratio of the space densities of AGN in the column-density intervals $N_H = 10^{22} - 10^{24} \text{ cm}^{-2}$ and $10^{20} - 10^{24} \text{ cm}^{-2}$. The results are presented in Table 4 and are plotted in Figure 14. We find that the observed Compton-thin AGN fraction in the luminosity interval $\log L_X(2 - 10 \text{ keV})/\text{erg s}^{-1} = 43.5 - 44$ increases from $46 \pm_{-12}^{+11} \%$ at a mean redshift $z = 0.25$ to $75 \pm_{-5}^{+5} \%$

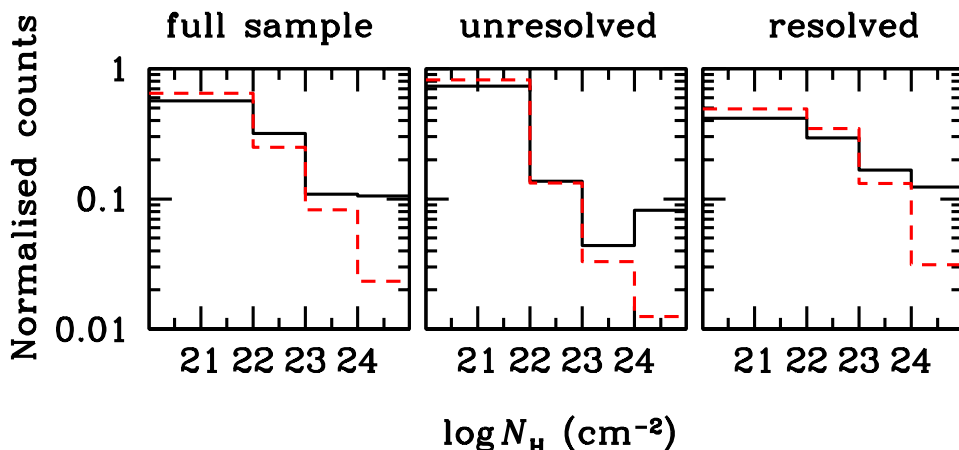


Figure 10. Observed hydrogen column density distribution for the XMM-XXL-N hard X-ray selected sample. This black solid histogram is estimated by summing the $\log N_H$ posterior probability distribution functions of individual sources. The red dashed histogram weights the posterior distribution of individual sources with the corresponding value of the X-ray luminosity function (equation 5), and therefore provides a more representative view of the detected AGN population in the XMM-XXL-N survey. The left panel presents the full sample, the middle panel corresponds to X-ray sources with optically unresolved (point-like) counterparts and the right panel is for X-ray sources with optically resolved (extended light profile) counterparts.

at a mean redshift $z = 1.25$. At brighter luminosities, $L_X(2 - 10 \text{ keV}) > 10^{44} \text{ erg s}^{-1}$, this fraction is found to be about 35% independent of redshift. Figure 14 also compares our results with recent constraints in the literature (Merloni et al. 2014; Ueda et al. 2014; Buchner et al. 2015; Aird et al. 2015a). Within the uncertainties there is reasonable agreement with previous estimates. It is also worth emphasising the smaller uncertainties of the XMM-XXL-N data points at $L_X(2 - 10 \text{ keV}) \gtrsim 10^{44} \text{ erg s}^{-1}$ compared to previous studies. This demonstrates the complementarity of deep *Chandra* and wide/shallow *XMM* surveys in studies of the distribution of AGN in obscuration over a wide luminosity baseline.

4.2 Comparison with infrared-selected AGN

Next it is investigated if the total space density of X-ray AGN, including obscured sources, is consistent with constraints from infrared-selected samples. Like in the X-ray, AGN selected at these longer wavelengths are less prone to the effects of obscuration, albeit with non-negligible levels of contamination by non-AGN sources. For this exercise the X-ray luminosity function is integrated in the range $N_H = 10^{20} - 10^{24} \text{ cm}^{-2}$ (i.e. only Compton-thin sources) to avoid current uncertainties in the determination of the space density of Compton thick AGN. We also adopt the most recent results on the space density of infrared-selected AGN presented by Delvecchio et al. (2014). They fit galaxy and AGN templates to the multi-waveband spectral energy distribution of *Herschel* infrared-selected galaxies in the GOODS-South (Great Observatories Origins Deep Survey-South, Elbaz et al. 2011) and the COSMOS fields to identify those with a statistically significant AGN component. These are then used to constrain the space density of AGN, including heavily obscured systems, as a function of bolometric AGN luminosity inferred from the SED fits. We use the parametric AGN luminosity functions at different redshifts provided by Delvecchio et al. (2014) to interpolate

to the mean of the three redshift intervals adopted in this paper. Bolometric luminosities are converted to X-ray luminosities using the bolometric corrections of Marconi et al. (2004). These results are plotted in Figure 15.

There is broad agreement between the X-ray luminosity function of Compton-thin X-ray selected AGN and that of infrared-selected ones, given the current level of uncertainties in the determination of AGN space densities, and systematics associated with e.g. the conversion from bolometric to X-ray luminosities. Additionally, the level of agreement between the X-ray and infrared luminosity functions argues against a large population of heavily obscured sources that are identified at the infrared and are missing from X-ray wavelengths. The addition of Compton thick AGN to the X-ray luminosity function constraints in Figure 15 would further strengthen this argument. Assuming for example a flat 30% fraction of Compton thick AGN independent of redshift and luminosity (Buchner et al. 2015) would shift the X-ray curves and data-points in Figure 15 upward by about 0.15 dex.

Next we explore the completeness of infrared colour-selection methods proposed in the literature to identify obscured and luminous AGN, using as starting point the XMM-XXL-N AGN sample. Figure 16 plots the distribution of XMM-XXL-N AGN in the 2-dimensional plane that consists of WISE $W_1 - W_2$ infrared colour and X-ray luminosity. Different panels correspond to different redshift and hydrogen column-density intervals. The density contours in that figure are constructed using the redshift, luminosity and column density probability distribution functions derived from the X-ray spectral analysis of individual sources. A single source may therefore spread out in different luminosity and redshift bins. Iso-density curves correspond to the 68th and 95th percentile of the distribution.

We adopt the colour limit $W_1 - W_2 > 0.8$ defined by Stern et al. (2012) for selecting AGN. Formally their selection also includes a magnitude cut in the WISE W_2 filter, $W_2 < 15.05 \text{ mag}$. This is primarily driven by the depth of

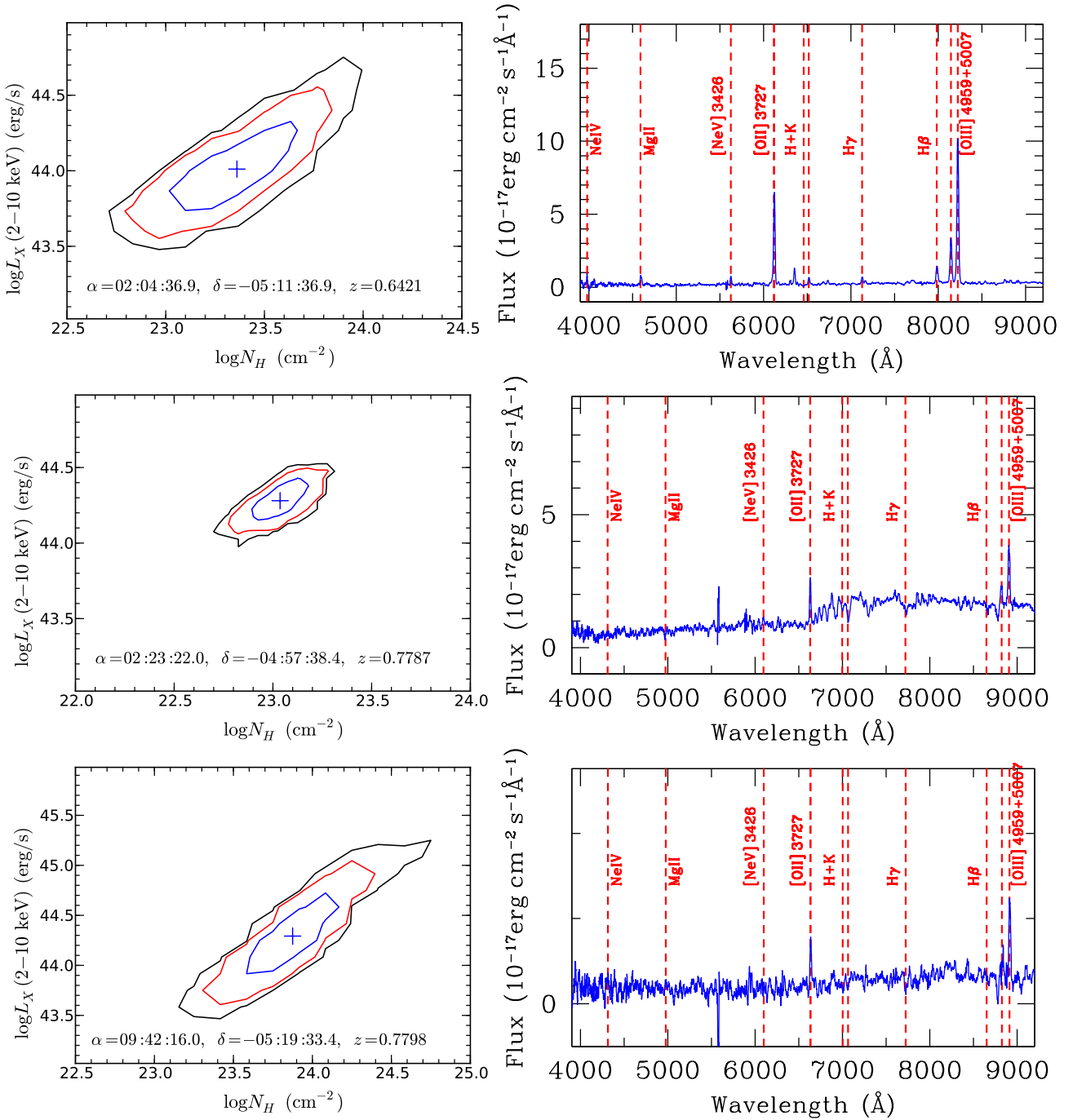


Figure 11. Examples of X-ray spectral constraints and SDSS optical spectra of three relatively luminous, obscured X-ray selected AGN in the XMM-XXL-N field with available SDSS spectroscopy. The panels on the left show the posterior probability distribution function in the two-dimensional space of intrinsic X-ray luminosity in the 2–10 keV band and the line-of-sight hydrogen column density inferred from the X-ray spectral analysis. The median luminosity and column density are marked by the cross. The contours enclose 68 (blue), 95 (red) and 99% (black) of the posterior probability distribution. The right panels show the SDSS optical spectra of each source. The redshift (z) and sky coordinates of the optical counterpart of each X-ray source are also shown.

the WISE observations in the COSMOS field, which was used to calibrate the WISE AGN selection, and the requirement to minimise contamination. Our work uses the deeper AllWISE catalogue. Additionally, contamination is not an issue since all the X-ray sources in the sample are AGN. Figure 16 shows that the fraction of sources that pass the

cut $W_1 - W_2 > 0.8$ changes primarily with redshift. The impacts of obscuration and X-ray luminosity appear to be second-order effects. We caution, nevertheless, that the luminosity baseline of our sample is not large. The fraction of X-ray selected AGN above the WISE colour cut proposed by Stern et al. (2012) increases from about 20–30% at $z < 0.5$

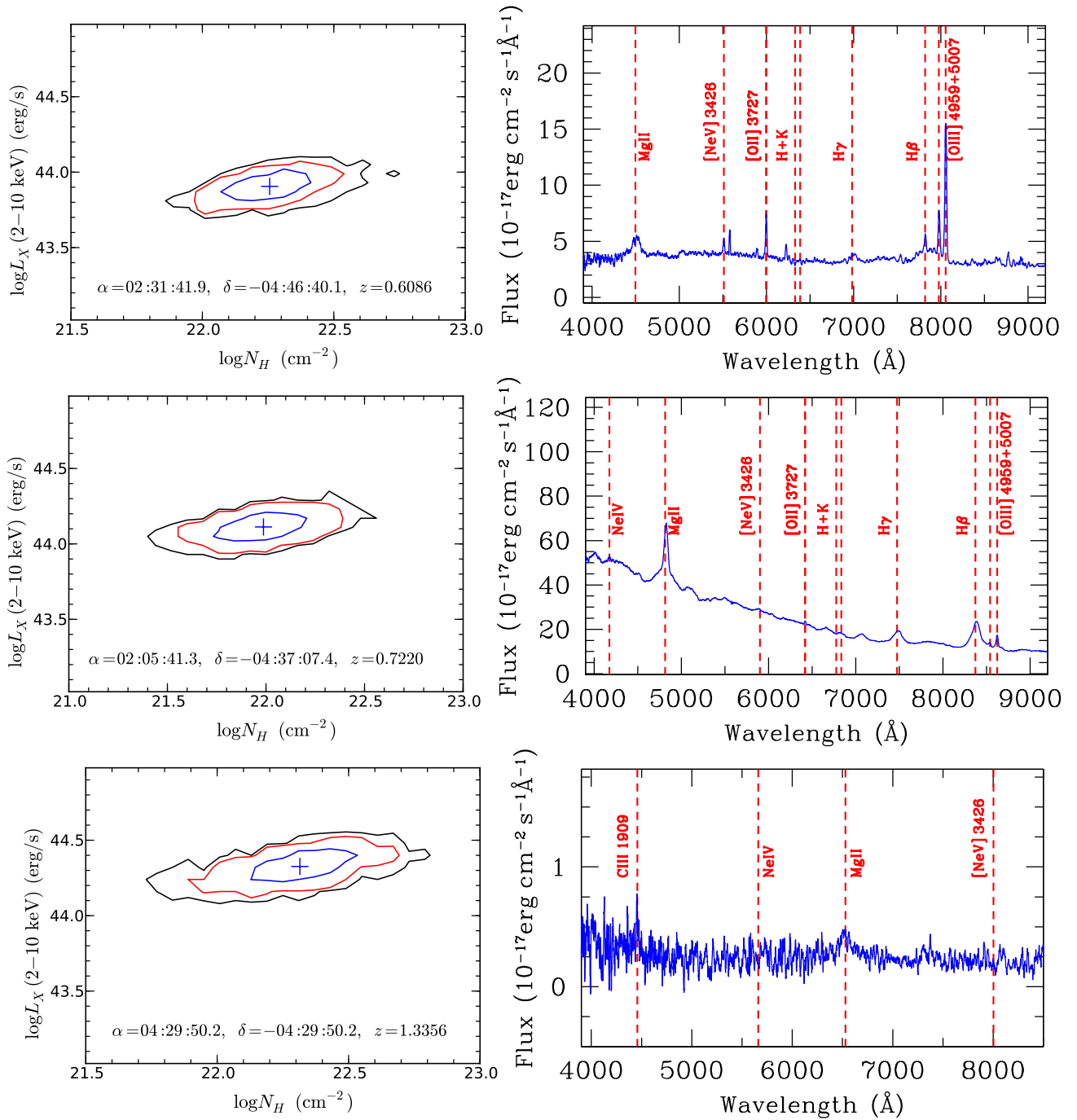


Figure 12. Examples of XMM-XXL-N AGN with broad optical emission-line spectra and evidence for X-ray obscuration, $N_H \gtrsim 10^{22} \text{ cm}^{-2}$. The panels on the left show the posterior probability distribution in the two-dimensional space of intrinsic X-ray luminosity in the 2-10 keV band and the line-of-sight hydrogen column density inferred from the X-ray spectral analysis. The median luminosity and column density are marked by the cross. The contours enclose 68 (blue), 95 (red) and 99% (black) of the posterior distribution function. The right panels show the SDSS optical spectra of each source. The redshift (z) and sky coordinates of the optical counterpart of each X-ray source are also shown.

to $> 50\%$ at $z > 1$ with some variation among column density bins at fixed redshift. Similar conclusions apply to the AGN mid-IR selection criteria proposed by Donley et al. (2012). Figure 17 shows how the XMM-XXL-N X-ray selected AGN are distributed on Spitzer mid-IR colour-colour plane relative to the selection wedge proposed by Donley

et al. (2012). The fraction of XMM-XXL-N AGN within that wedge increases from about 20-30% at $z \approx 0.5$ to 60-70% at $z \approx 1.5$. These fractions are not particularly sensitive to intrinsic AGN X-ray luminosity cuts.

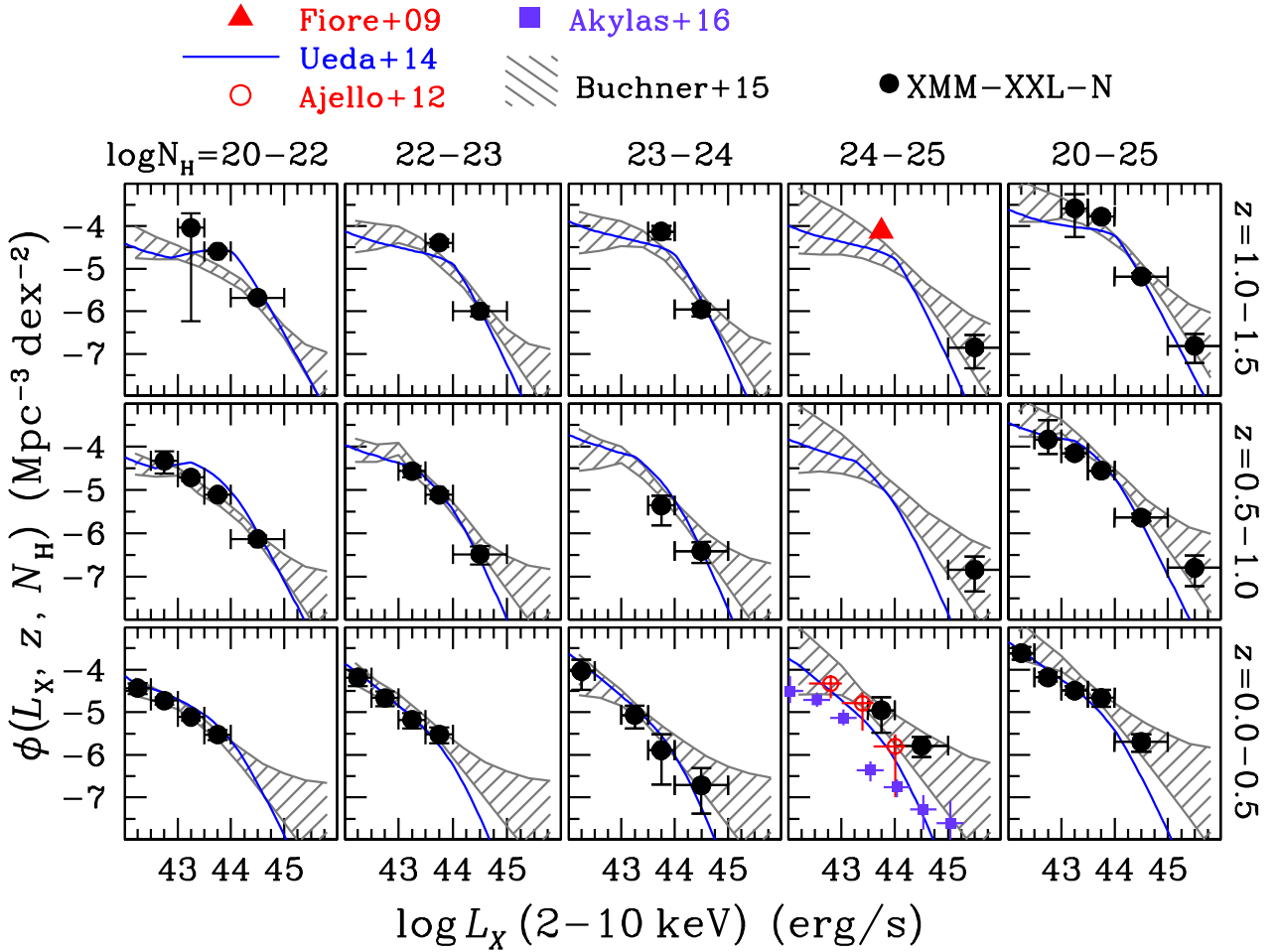


Figure 13. Space density of AGN per luminosity and column density decades (i.e. in units of $\text{Mpc}^{-3} \text{dex}^{-2}$). Different panels correspond to different levels of line-of-sight obscuration (left to right) and different redshift intervals (bottom: $z = 0.0 - 0.5$; middle: $z = 0.5 - 1.0$; top: $z = 1.0 - 1.5$). The last column of panels plots the total luminosity function, i.e. integrated across the hydrogen column density interval $N_H = 10^{20} - 10^{25} \text{ cm}^{-2}$. Black data points (filled circles) are the non-parametric space density estimates using the XMM-XXL-N data. The uncertainties in the vertical direction correspond to the 90% percentiles around the median of the space density probability distribution function. The horizontal error-bars show the luminosity bin size. The XXL data points are compared with the XLF estimates of Buchner et al. (2015, grey hatched regions), Ueda et al. (2014, blue curves) and in the case of low redshift Compton-thick AGN with the local Swift/BAT constraints of Ajello et al. (2012, red circles) and Akylas et al. (2016, purple squares). The red triangle in the $z = 1.0 - 1.5$ Compton thick panel is the space density estimated by Fiore et al. (2009) for infrared-selected Compton thick AGN candidates in the redshift interval $z = 0.7 - 1.2$.

4.3 Comparison with UV-selected AGN

In this section the space density of unobscured X-ray selected AGN is compared to that of UV-selected QSOs. In the X-ray literature unobscured AGN are often defined as those with column densities $N_H < 10^{22} \text{ cm}^{-2}$. Recent evidence suggests that the consistency between optically-classified type-1 AGN and X-ray unobscured ones is maximised at a lower threshold, $\log N_H = 10^{21.5} \text{ cm}^{-2}$ (Merloni et al. 2014; Liu et al. 2016). This limit is adopted here to compare the luminosity functions of X-ray and UV/optically-selected AGN samples. The space density of X-ray unobscured AGN (i.e. $\log N_H/\text{cm}^2 = 20 - 21.5$) is then approximated by simply scaling the estimated space densities in the logarithmic interval $\log N_H/\text{cm}^2 = 20 - 22$ by a factor of 1.5. The underlying assumption is a flat distribution of AGN in the logarithmic column density interval $\log N_H/\text{cm}^2 = 20 - 22$. For

the luminosity of UV/optically-selected QSOs we use the LEDE (Luminosity and Density Evolution) parametrisation of Croom et al. (2009), which is constrained by observations in the redshift interval $0.4 - 1.5$. The conversion of QSO absolute optical magnitudes to X-ray luminosities follows the steps described in Croom et al. (2009). At lower redshift, $z < 0.4$, we also compare our results with the broad-line AGN luminosity function presented by Schulze et al. (2009). From the latter study we use the double power-law parametrisation of the redshift $z = 0$ bolometric luminosity function. This is converted to X-rays using the Marconi et al. (2004) bolometric corrections. Following Schulze et al. (2009) pure density evolution of the form $(1+z)^5$ is also included to determine the broad-line AGN luminosity function at redshifts $z > 0$. The comparison between X-ray and optical type-1 AGN luminosity functions is presented in Figure 18. Overall there is fair agreement between the space

densities of unobscured ($\log N_{\text{H}}/\text{cm}^2 = 20 - 21.5$) X-ray selected AGN and UV/optically selected QSOs. At low redshift the [Schulze et al. \(2009\)](#) luminosity function appears to exceed the X-ray space densities of unobscured AGN below about $L_X(2 - 10 \text{ keV}) \approx 10^{43} \text{ erg s}^{-1}$. A similar trend has been reported by [Schulze et al. \(2009\)](#) when comparing their luminosity function with the soft-band (0.5-2 keV) X-ray luminosity function of [Hasinger et al. \(2005\)](#). A possible explanation is that the faint-end of the [Schulze et al. \(2009\)](#) luminosity function includes a fraction of Seyfert-1.8s and 1.9s, i.e. not purely type-1 AGN. These sources correspond to a higher X-ray column density threshold, e.g. $\log N_{\text{H}}/\text{cm}^2 \approx 22.3$ ([Burtscher et al. 2016](#)). Differences in e.g. the adopted bolometric corrections or the definition of type-1 AGN may also contribute to the difference between the faint-end of the [Schulze et al. \(2009\)](#) and X-ray luminosity functions.

4.4 eROSITA predictions

Finally we explore expectations from the eROSITA All Sky Survey on the determination of the AGN space density as a function of redshift, accretion luminosity and line-of-sight hydrogen column density. For this exercise we assume (i) that the AGN population follows the median space density constraints of [Buchner et al. \(2015\)](#), (ii) the uncertainty of the luminosity function scales as $\delta\phi(L_X, z, N_H)/\phi(L_X, z, N_H) \propto 1/\sqrt{N}$, where N is the expected number of AGN in a given (L_X, z, N_H) bin, (iii) the 4-year depth of the eROSITA All Sky Survey in the soft-band, $f_X(0.5 - 2 \text{ keV}) = 1.5 \times 10^{-14} \text{ erg s}^{-1} \text{ cm}^{-2}$ ([Merloni et al. 2012](#)), over a total area of 5000 deg^2 , (iii) the X-ray spectral model described in section 2.5 with $\Gamma = 1.9$ and the normalisations of the soft power-law and reflection components fixed to 10% and 1% respectively, of the normalisation of the intrinsic power-law spectrum.

The resulting eROSITA predictions are plotted in Figure 19 along with the non-parametric constraints of the AGN space density from [Buchner et al. \(2015\)](#) and the XMM-XXL-N. This figure shows that the eROSITA will provide excellent statistics for AGN population studies at redshifts $z \lesssim 0.5$ over a range of X-ray luminosities, $L_X(2 - 10 \text{ keV}) \approx 10^{43} - 10^{45} \text{ erg s}^{-1}$, and for column densities approaching the Compton thick limit, $N_{\text{H}} \approx 10^{24} \text{ cm}^{-2}$. We choose not to provide eROSITA predictions for Compton-thick AGN because current measurements remain somewhat uncertain and the detectability of such heavily obscured sources by the eROSITA All Sky Survey is sensitive to the adopted AGN X-ray spectral model, and in particular the level of the soft scattering component (see also [Akylas et al. 2012](#)). At redshifts $z > 0.5$ the eROSITA All Sky Survey will be sensitive to moderate obscured AGN, $N_{\text{H}} \lesssim 10^{23} \text{ cm}^{-2}$, at the bright-end of the luminosity function $L_X(2 - 10 \text{ keV}) \gtrsim 10^{44} \text{ erg s}^{-1}$. At higher levels of obscurations only the most extreme sources in terms of luminosity are expected to be detected, $L_X(2 - 10 \text{ keV}) \gtrsim 10^{45} \text{ erg s}^{-1}$.

We caution that the eROSITA predictions plotted in Figure 19 only depend on the expected number of AGN in different (L_X, z, N_H) bins. They do not account for uncertainties in the determination of redshifts (e.g. via photometric methods), the measurement errors of the line-of-sight col-

umn density from the X-ray spectra or uncertainties in the determination of the AGN space density at the bright end of the luminosity function from current surveys.

5 DISCUSSION

This paper presents constraints on the space density of obscured AGN at relatively high accretion luminosities, $L_X(2 - 10 \text{ keV}) \approx 10^{44} \text{ erg s}^{-1}$, using one of the largest contiguous X-ray surveys currently available, in the equatorial XMM-XXL field. We show that despite the relatively shallow X-ray depth ($f_X(2 - 10 \text{ keV}) \approx 3 \times 10^{-15} \text{ erg s}^{-1} \text{ cm}^{-2}$; [Liu et al. 2016](#)), this sample provides robust estimates of the space density of Compton-thin ($N_{\text{H}} < 10^{24} \text{ cm}^{-2}$) AGN at luminosities close to and above the break of the luminosity function ($L_X(2 - 10 \text{ keV}) \approx 10^{44} \text{ erg s}^{-1}$; [Aird et al. 2010](#); [Ueda et al. 2014](#); [Aird et al. 2015a](#)), where smaller area X-ray surveys are affected by small number statistics. This point is demonstrated in Figure 9, from which it can be inferred that the XMM-XXL improves by a factor of four the number of AGN with $L_X(2 - 10 \text{ keV}) > 10^{44} \text{ erg s}^{-1}$ and $z < 1.5$ compared to the combined Chandra COSMOS, AEGIS-XD and CDFS-4Ms samples presented by [Buchner et al. \(2015\)](#). For heavily obscured, Compton-thick AGN, the XMM-XXL-N provides constraints only in the case of very luminous sources, i.e. $L_X(2 - 10 \text{ keV}) > 10^{45} \text{ erg s}^{-1}$ at $z > 0.5$. Additional observations at rest-frame energies $> 10 \text{ keV}$ are also needed to complement existing X-ray spectroscopy below about 10 keV and confirm the high levels of line-of-sight obscuration of these systems. Therefore the Compton thick AGN space density constraints from the XMM-XXL-N sample should be viewed with caution.

We estimate a Compton-thin obscured AGN fraction of ≈ 0.35 for luminosities $\log L_X(2 - 10 \text{ keV}) = 44 - 45 \text{ erg s}^{-1}$ independent of redshift to $z \approx 1.5$. At somewhat fainter luminosities [$\log L_X(2 - 10 \text{ keV}) = 43.75 \text{ erg s}^{-1}$] there is evidence that the obscured AGN fraction increases with redshift from 0.45 ± 0.10 at $z = 0.25$ to 0.75 ± 0.05 at $z = 1.25$. Similar results are claimed by [Buchner et al. \(2015\)](#) who show that the Compton-thin AGN fraction is a complex function of accretion luminosity and redshift. At high accretion luminosities [$\log L_X(2 - 10 \text{ keV}) > 44 \text{ erg s}^{-1}$] feedback process associated with AGN winds may be responsible for clearing dust and gas clouds in the vicinity of supermassive black holes and hence, lowering the obscured AGN fraction. At lower accretion luminosities [$\log L_X(2 - 10 \text{ keV}) < 44 \text{ erg s}^{-1}$] AGN feedback is likely subdominant. The increase of the obscured AGN fraction with redshift at lower luminosities may be associated with the overall increase in the dust content of galaxies with redshift, which in turn is linked to the higher specific star-formation rates of galaxies at earlier epochs (e.g. [Noeske et al. 2007](#); [Magdis et al. 2012](#); [Santini et al. 2014](#)).

We also show that infrared surveys that identify AGN via template fits to the observed multi-waveband Spectral Energy Distribution ([Delvecchio et al. 2014](#)) estimate AGN luminosity functions that are broadly consistent with the space densities of Compton-thin AGN determined in the XMM-XXL-N at high accretion luminosities [$\log L_X(2 - 10 \text{ keV}) \gtrsim 43 \text{ erg s}^{-1}$]. This comparison is limited by the current level of random uncertainties in the AGN space den-

sities at both X-ray and infrared wavelengths and the level of contribution of Compton thick AGN to the X-ray luminosity function. Despite these points the level of agreement between X-ray and infrared AGN luminosity functions is evidence against a large population of obscured sources that is identified by infrared selection methods but is missing at X-ray wavelengths. For example, in Figure 13 there is reasonable agreement between the space density of Compton thick AGN candidates estimated using either X-ray or mid-infrared (Fiore et al. 2009) selected samples at $z \approx 1$. Similar conclusions are also presented by Buchner et al. (2015) by comparing X-ray constraints with infrared selected samples of Compton thick AGN (Fiore et al. 2008, 2009; Alexander et al. 2011) to redshift $z \approx 2$. Despite the current level of agreement between the space densities of X-ray and infrared selected AGN, a population of deeply buried sources that remains unidentified at both wavelengths cannot be excluded.

It is further shown that selecting AGN using mid-IR colour cuts only (e.g. Donley et al. 2012; Stern et al. 2012) leads to redshift-dependent incompleteness. Nevertheless, at $z \gtrsim 1$ these methods are efficient and relatively complete ($\approx 50 - 70\%$) in compiling luminous AGN samples including heavily obscured systems. Stern et al. (2012) used AGN and galaxy template Spectral Energy Distributions to investigate the redshift-dependent efficiency of the AGN selection based on the WISE $W1 - W2$ colour. They showed that suppression of the AGN mid-infrared emission relative to the host galaxy, either because of dust extinction or dilution by stellar light, is an issue for redshifts $z \lesssim 1.5$. Stern et al. (2012) showed that the exact redshift dependence of the $W1 - W2$ colour-selection efficiency depends on the levels of extinction and dilution of the AGN radiation. For example, templates with AGN emission fraction of 50% in the wavelength range $0.1 - 30 \mu\text{m}$ lie below the colour cut $W1 - W2 = 0.8$ used to select AGN at all redshifts below $z = 1.5$. An AGN fraction in the wavelength range $0.1 - 30 \mu\text{m}$ of 75% reduces the efficiency of selecting AGN via the colour cut $W1 - W2 = 0.8$ only in the relatively narrow redshift range $z \approx 0.5 - 1$. The redshift dependent incompleteness in Figure 16 is likely related to the above effects, with lower redshift AGN being more diluted than higher redshift sources. Interestingly the level of the line-of-sight obscuration measured by $\log N_H$ appears to be a second order effect on the incompleteness fractions of Figure 16. This may be because at fixed redshift more obscured sources in the flux limited XMM-XXL-N sample are also expected to have higher X-ray luminosities and therefore a larger contrast of the integrated AGN emission relative to the host galaxy.

Applying a hydrogen column density cut $\log N_H/\text{cm}^2 = 21.5$ to the X-ray sample we find fair agreement with the luminosity functions of UV/optically-selected QSO, particularly at $z \gtrsim 0.5$. This is consistent with independent claims that the column density threshold that maximises the agreement between the X-ray unobscured and the UV/optically-selected broad-line QSO classes is $\log N_H/\text{cm}^2 = 21.5$ (e.g. Merloni et al. 2014). The XMM-XXL-N sample also includes a small fraction (10% Liu et al. 2016) of AGN with broad optical emission lines and evidence for X-ray obscuration higher than $N_H \gtrsim 10^{22} \text{cm}^{-2}$ (see Fig. 12). This fraction is similar to previous estimates in the literature (e.g. Brusa et al. 2003). These sources likely include a fraction of type-1.8 or earlier Seyferts, which at least in the local Universe

are associated, on the average, with hydrogen columns in excess of $N_H = 10^{22} \text{cm}^{-2}$ (Burtscher et al. 2016). The class of Broad Absorption Line (BAL) QSOs is known to be X-ray underluminous for their UV emission likely because of X-ray obscuration along the line-of-sight but also, in few cases, because of an intrinsically weak X-ray continuum (e.g. Gallagher et al. 2006; Gibson et al. 2009; Luo et al. 2013, 2014). The fraction of BAL features among optical/UV-selected QSOs can be as high as 26% (Hewett & Foltz 2003; Reichard et al. 2003; Gibson et al. 2009). Stalin et al. (2011) studied the incidence of BAL troughs among X-ray selected AGN in the XMM-LSS sample and reported a fraction of $7 \pm 5\%$, i.e. lower than optical/UV-selected QSOs but comparable to the fraction of XMM-XXL-N broad-line QSOs with X-ray absorption $N_H \gtrsim 10^{22} \text{cm}^{-2}$ (10% Liu et al. 2016). Searching for BAL features in the optical spectra of the present X-ray sample is beyond the scope of this paper. Nevertheless, it is interesting that one of the type-1 and X-ray absorbed sources in Figure 12 ($\alpha = 02 : 05 : 41.3$, $\delta = -0.4 : 37 : 07.4$, $z = 0.7220$) shows evidence for an absorption trough blueward of the Mg II broad emission line.

Finally, we make predictions on the AGN space density constraints that the eROSITA All Sky Survey (Merloni et al. 2012) can deliver. We show that this mission will provide a nearly unbiased census of AGN, including heavily obscured systems approaching column densities $N_H \approx 10^{24} \text{cm}^{-2}$, at relatively low redshift $z < 0.5$ and for accretion luminosities $L_X \gtrsim 10^{43} \text{erg s}^{-1}$. This sample will be a unique resource for studying AGN demographics and population properties at $z < 0.5$, i.e. in the last 5 Gyrs of cosmic time. At higher redshifts eROSITA will place unique constraints on the bright-end of the luminosity function ($L_X \gtrsim 10^{44} \text{erg s}^{-1}$) and the fraction of moderately obscured sources among such luminous AGN.

ACKNOWLEDGEMENTS

We thank the anonymous referee for useful comments and suggestions. This work benefited from the THALES project 383549 that is jointly funded by the European Union and the Greek Government in the framework of the programme ‘‘Education and lifelong learning’’. We acknowledge support from the FONDECYT Postdoctorados 3160439 (JB) and the Ministry of Economy, Development, and Tourism’s Millennium Science Initiative through grant IC120009, awarded to The Millennium Institute of Astrophysics MAS (JB). Funding for SDSS-III has been provided by the Alfred P. Sloan Foundation, the Participating Institutions, the National Science Foundation, and the U.S. Department of Energy Office of Science. The SDSS-III web site is <http://www.sdss3.org/>. SDSS-III is managed by the Astrophysical Research Consortium for the Participating Institutions of the SDSS-III Collaboration including the University of Arizona, the Brazilian Participation Group, Brookhaven National Laboratory, Carnegie Mellon University, University of Florida, the French Participation Group, the German Participation Group, Harvard University, the Instituto de Astrofísica de Canarias, the Michigan State/Notre Dame/JINA Participation Group, Johns Hopkins University, Lawrence Berkeley National Laboratory, Max Planck Institute for Astrophysics, Max Planck Institute for Extraterrestrial Physics,

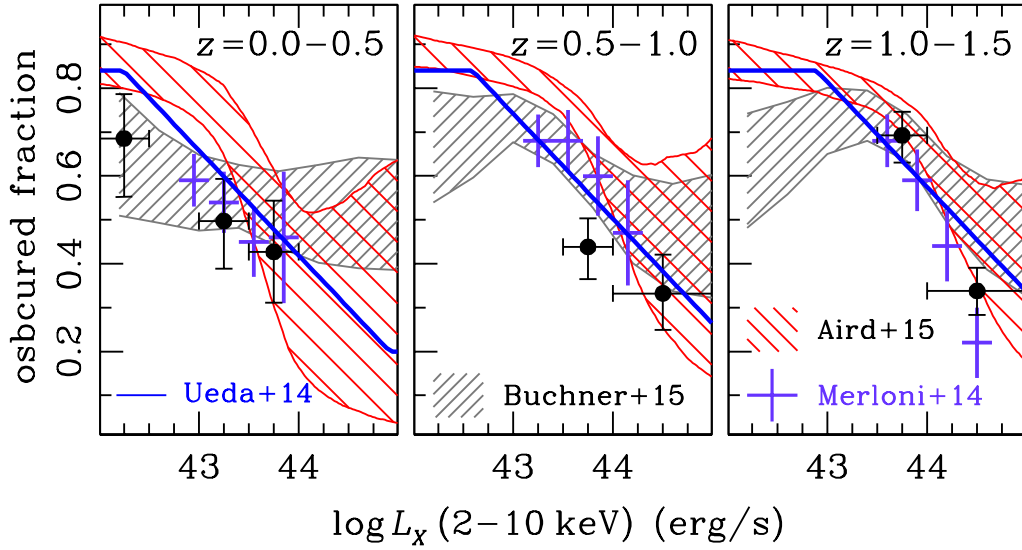


Figure 14. Fraction of obscured (Compton-thin) AGN as a function of luminosity. The obscured fraction is the ratio of the AGN space density in the line-of-sight column density intervals $\log N_H = 22 - 24$ and $\log N_H = 20 - 24$ (in units of cm^{-2}). Different panels correspond to different redshift intervals (left: $z = 0.0 - 0.5$; middle $z = 0.5 - 1.0$; right $z = 1.0 - 1.5$). The black data points are inferred from the non-parametric space density estimates using the XMM-XXL-N data. The uncertainties in the vertical direction correspond to the 90% percentiles around the median of the probability distribution function. The horizontal error-bars show the luminosity bin size. The XMM-XXL-N constraints are compared with the obscured fractions determined by Buchner et al. (2015; grey hatched regions), Aird et al. (2015; red hatched regions), Ueda et al. (2014; blue curves) and Merloni et al. (2014; purple crosses).

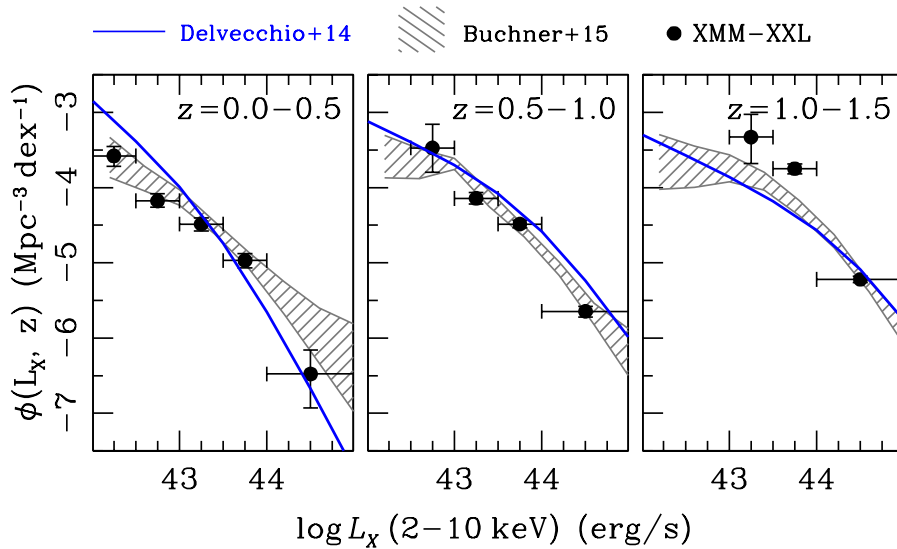


Figure 15. Total X-ray luminosity function of Compton-thin AGN, $N_H = 10^{20} - 10^{24} \text{ cm}^{-2}$ (space density per luminosity decade). The black datapoints are the constraints from the XMM-XXL-N, the shaded area represents the recent results of Buchner et al. (2015). The blue curve is the luminosity function of infrared-selected AGN estimated by Delvecchio et al. (2014).

New Mexico State University, New York University, Ohio State University, Pennsylvania State University, University of Portsmouth, Princeton University, the Spanish Participation Group, University of Tokyo, University of Utah, Vanderbilt University, University of Virginia, University of Washington, and Yale University.

REFERENCES

- Aihara H., et al., 2011, *ApJS*, **193**, 29
 Aird J., et al., 2010, *MNRAS*, **401**, 2531
 Aird J., Coil A. L., Georgakakis A., Nandra K., Barro G., Pérez-González P. G., 2015a, *MNRAS*, **451**, 1892
 Aird J., et al., 2015b, *ApJ*, **815**, 66
 Ajello M., Alexander D. M., Greiner J., Madejski G. M., Gehrels N., Burlon D., 2012, *ApJ*, **749**, 21
 Akylas A., Georgantopoulos I., 2009, *A&A*, **500**, 999
 Akylas A., Georgantopoulos I., Georgakakis A., Kitsionas S.,

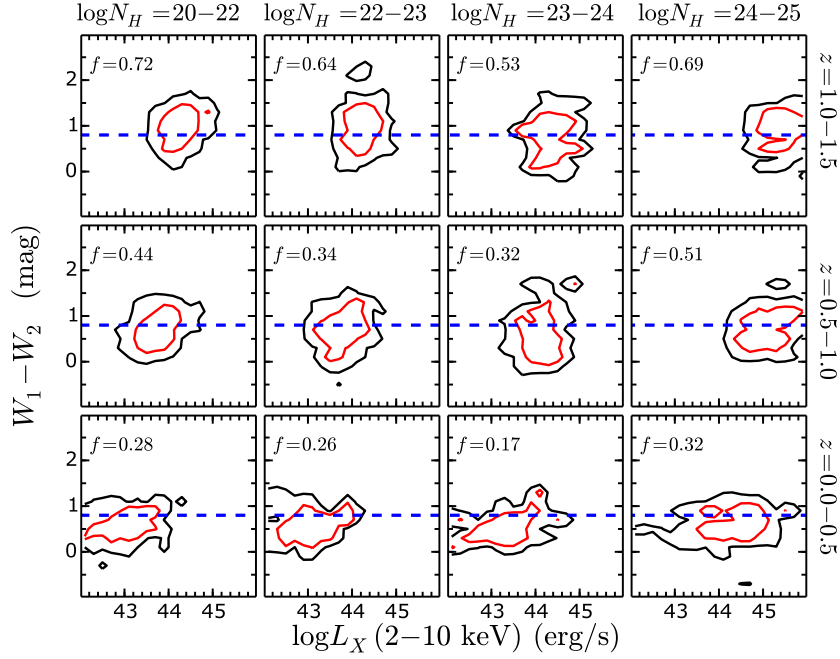


Figure 16. WISE $W_1 - W_2$ infrared colour as a function 2-10 keV X-ray luminosity for XMM-XXL-N X-ray selected AGN. The contours show density of AGN and the different panels correspond to different redshifts and column density intervals as indicated by labels at the top and the right of the panels. The contours are constructed using the probability distribution function of individual XMM-XXL-N sources in redshift, luminosity and column density. The iso-density contours correspond to the 68th and 95th percentile of the distribution. The vertical dashed line indicates the Stern et al. (2012) WISE AGN colour selection. The numbers in each panel indicate the fraction, f , of X-ray sources above the Stern et al. (2012) WISE AGN colour cut.

- Hatziminaoglou E., 2006, *A&A*, 459, 693
 Akylas A., Georgakakis A., Georgantopoulos I., Brightman M., Nandra K., 2012, *A&A*, 546, A98
 Akylas A., Georgantopoulos I., Ranalli P., Gkiokas E., Corral A., Lanzuisi G., 2016, *A&A*, 594, A73
 Alam S., et al., 2015, *ApJS*, 219, 12
 Alexander D. M., et al., 2011, *ApJ*, 738, 44
 Alexander D. M., et al., 2013, *ApJ*, 773, 125
 Arnouts S., Cristiani S., Moscardini L., Matarrese S., Lucchin F., Fontana A., Giallongo E., 1999, *MNRAS*, 310, 540
 Barger A. J., Cowie L. L., Mushotzky R. F., Yang Y., Wang W.-H., Steffen A. T., Capak P., 2005, *AJ*, 129, 578
 Barthelmy S. D., et al., 2005, *Space Sci.Rev.*, 120, 143
 Bianchi L., Efremova B., Herald J., Girardi L., Zobot A., Marigo P., Martin C., 2011, *MNRAS*, 411, 2770
 Bradshaw E. J., et al., 2013, *MNRAS*, 433, 194
 Brand K., et al., 2006, *ApJ*, 641, 140
 Brandt W. N., Alexander D. M., 2015, *A&A Rev.*, 23, 1
 Brightman M., Nandra K., 2011a, *MNRAS*, 413, 1206
 Brightman M., Nandra K., 2011b, *MNRAS*, 414, 3084
 Brightman M., Nandra K., 2012, *MNRAS*, 422, 1166
 Brightman M., Ueda Y., 2012, *MNRAS*, 423, 702
 Brusa M., et al., 2003, *A&A*, 409, 65
 Brusa M., et al., 2007, *ApJS*, 172, 353
 Buchner J., et al., 2014, *A&A*, 564, A125
 Buchner J., et al., 2015, *ApJ*, 802, 89
 Burlon D., Ajello M., Greiner J., Comastri A., Merloni A., Gehrels N., 2011, *ApJ*, 728, 58
 Burtscher L., et al., 2016, *A&A*, 586, A28
 Calzetti D., Armus L., Bohlin R. C., Kinney A. L., Koornneef J., Storchi-Bergmann T., 2000, *ApJ*, 533, 682
 Carpenter O., et al., 2016, *Journal of Statistical Software*, in press
 Ciliegi P., Zamorani G., Hasinger G., Lehmann I., Szokoly G., Wilson G., 2003, *A&A*, 398, 901
 Civano F., et al., 2016, *ApJ*, 819, 62
 Clerc N., et al., 2014, *MNRAS*, 444, 2723
 Comastri A., Setti G., Zamorani G., Hasinger G., 1995, *A&A*, 296, 1
 Croom S. M., et al., 2009, *MNRAS*, 399, 1755
 Cross N. J. G., et al., 2012, *A&A*, 548, A119
 Della Ceca R., et al., 2008, *A&A*, 487, 119
 Delvecchio I., et al., 2014, *MNRAS*, 439, 2736
 Donley J. L., et al., 2012, *ApJ*, 748, 142
 Draper A. R., Ballantyne D. R., 2009, *ApJ*, 707, 778
 Dunne L., et al., 2011, *MNRAS*, 417, 1510
 Ebrero J., et al., 2009, *A&A*, 493, 55
 Elbaz D., et al., 2011, *A&A*, 533, A119
 Elvis M., et al., 2009, *ApJS*, 184, 158
 Emerson J., 2004, *The Observatory*, 124, 336
 Erben T., et al., 2013, *MNRAS*, 433, 2545
 Fabian A. C., 1999, *MNRAS*, 308, L39
 Fiore F., et al., 2008, *ApJ*, 672, 94
 Fiore F., et al., 2009, *ApJ*, 693, 447
 Gallagher S. C., Brandt W. N., Chartas G., Priddey R., Garmire G. P., Sambruna R. M., 2006, *ApJ*, 644, 709
 Garilli B., et al., 2014, *A&A*, 562, A23
 Georgakakis A., Nandra K., 2011, *MNRAS*, 414, 992
 Georgakakis A., Nandra K., Laird E. S., Aird J., Trichas M., 2008, *MNRAS*, 388, 1205
 Georgakakis A., et al., 2015, *MNRAS*, 453, 1946
 Gibson R. R., et al., 2009, *ApJ*, 692, 758
 Gilli R., Comastri A., Hasinger G., 2007, *A&A*, 463, 79
 Guainazzi M., Bianchi S., 2007, *MNRAS*, 374, 1290
 Gunn J. E., et al., 2006, *AJ*, 131, 2332

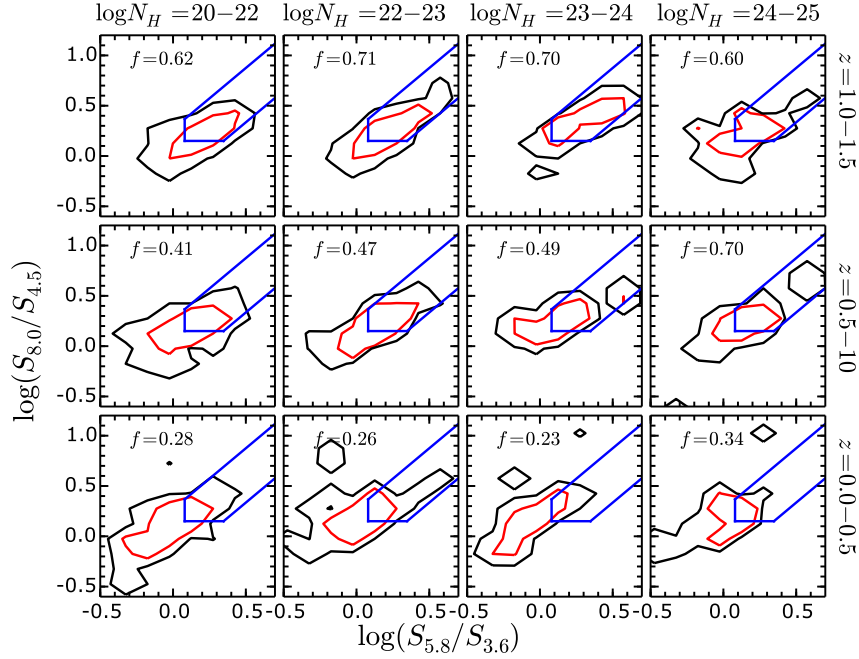


Figure 17. The Spitzer mid-infrared colour AGN selection plane proposed by [Donley et al. \(2012\)](#). The contours show density of XMM-XXL-N AGN and the different panels correspond to different redshifts and column density intervals as indicated by labels at the top and the right of the panels. The contours are constructed using the probability density function of individual XMM-XXL-N sources in redshift, luminosity and column density. The iso-density contours correspond to the 68th and 95th percentile of the distribution. The blue solid lines indicate the [Donley et al. \(2012\)](#) AGN selection wedge. The numbers in each panel indicate the fraction, f , of X-ray sources within the wedge.

- Guzzo L., et al., 2014, [A&A](#), **566**, A108
Hambly N. C., et al., 2008, [MNRAS](#), **384**, 637
Hasinger G., 2008, [A&A](#), **490**, 905
Hasinger G., Miyaji T., Schmidt M., 2005, [A&A](#), **441**, 417
Hewett P. C., Foltz C. B., 2003, [AJ](#), **125**, 1784
Heymans C., et al., 2012, [MNRAS](#), **427**, 146
Hopkins P. F., Hernquist L., Cox T. J., Di Matteo T., Robertson B., Springel V., 2006, [ApJS](#), **163**, 1
Hsu L.-T., et al., 2014, [ApJ](#), **796**, 60
Ilbert O., et al., 2006, [A&A](#), **457**, 841
Ilbert O., et al., 2009, [ApJ](#), **690**, 1236
Irwin M. J., et al., 2004, in Quinn P. J., Bridger A., eds, Proc. SPIE Vol. 5493, Optimizing Scientific Return for Astronomy through Information Technologies. pp 411–422, doi:10.1117/12.551449
Jarvis M. J., et al., 2013, [MNRAS](#), **428**, 1281
Kenter A., et al., 2005, [ApJS](#), **161**, 9
King A., 2003, [ApJ](#), **596**, L27
Kuntz K. D., Snowden S. L., 2010, [ApJS](#), **188**, 46
La Franca F., et al., 2005, [ApJ](#), **635**, 864
LaMassa S. M., Heckman T. M., Ptak A., 2012, [ApJ](#), **758**, 82
LaMassa S. M., Yaqoob T., Ptak A. F., Jia J., Heckman T. M., Gandhi P., Meg Urry C., 2014, [ApJ](#), **787**, 61
LaMassa S. M., et al., 2016, [ApJ](#), **817**, 172
Laird E. S., et al., 2009, [ApJS](#), **180**, 102
Lanzuisi G., et al., 2015, [A&A](#), **573**, A137
Le Fèvre O., et al., 2013, [A&A](#), **559**, A14
Liu Z., et al., 2016, [MNRAS](#), **459**, 1602
Luo B., et al., 2010, [ApJS](#), **187**, 560
Luo B., et al., 2013, [ApJ](#), **772**, 153
Luo B., et al., 2014, [ApJ](#), **794**, 70
Magdis G. E., et al., 2012, [ApJ](#), **760**, 6
Magdziarz P., Zdziarski A. A., 1995, [MNRAS](#), **273**, 837
Maggi P., et al., 2014, [A&A](#), **561**, A76
Marchesi S., et al., 2016, [ApJ](#), **817**, 34
Marconi A., Risaliti G., Gilli R., Hunt L. K., Maiolino R., Salvati M., 2004, [MNRAS](#), **351**, 169
McLure R. J., et al., 2013, [MNRAS](#), **428**, 1088
Menzel M.-L., et al., 2016, [MNRAS](#), **457**, 110
Merloni A., Heinz S., 2008, [MNRAS](#), **388**, 1011
Merloni A., et al., 2012, ArXiv e-prints 1209.3114,
Merloni A., et al., 2014, [MNRAS](#), **437**, 3550
Miyaji T., Hasinger G., Schmidt M., 2001, [A&A](#), **369**, 49
Nandra K., Pounds K. A., 1994, [MNRAS](#), **268**, 405
Nandra K., et al., 2015, arXiv 1503.09078,
Noeske K. G., et al., 2007, [ApJ](#), **660**, L47
Panessa F., Bassani L., Cappi M., Dadina M., Barcons X., Carrera F. J., Ho L. C., Iwasawa K., 2006, [A&A](#), **455**, 173
Pierre M., et al., 2015, ArXiv e-prints 1512.04317,
Press W. H., Teukolsky S. A., Vetterling W. T., Flannery B. P., 1992, Numerical recipes in FORTRAN. The art of scientific computing. Cambridge: University Press, |c1992, 2nd ed.
Prevot M. L., Lequeux J., Prevot L., Maurice E., Rocca-Volmerange B., 1984, [A&A](#), **132**, 389
Rangel C., Nandra K., Laird E. S., Orange P., 2013, [MNRAS](#), **428**, 3089
Reichard T. A., et al., 2003, [AJ](#), **125**, 1711
Risaliti G., Maiolino R., Salvati M., 1999, [ApJ](#), **522**, 157
Salvato M., et al., 2009, [ApJ](#), **690**, 1250
Salvato M., et al., 2011, [ApJ](#), **742**, 61
Santini P., et al., 2014, [A&A](#), **562**, A30
Schulze A., Wisotzki L., Husemann B., 2009, [A&A](#), **507**, 781
Silk J., Rees M. J., 1998, [A&A](#), **331**, L1
Soltan A., 1982, [MNRAS](#), **200**, 115

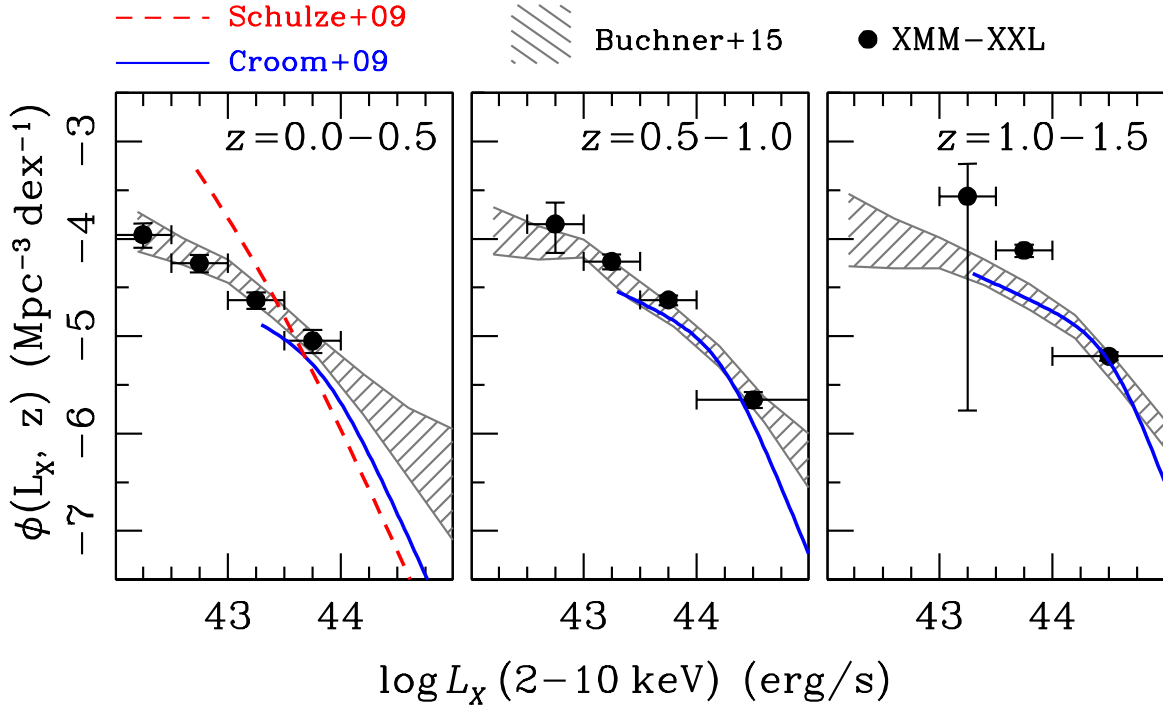


Figure 18. Space density per luminosity dex of X-ray selected unobscured AGN ($N_{\text{H}} = 10^{20} - 10^{21.5} \text{ cm}^{-2}$) in comparison with the luminosity function of UV/optical selected QSOs. The black data-points are the constraints from the XMM-XXL-N, the shaded area represents the results of Buchner et al. (2015). The blue curve is the LEDE (Luminosity Evolution and Density Evolution) parametrisation of UV/optical QSO luminosity function presented by Croom et al. (2009). The red dashed curve is the low redshift broad-line AGN luminosity function determined by Schulze et al. (2009). All the optically type-1 AGN luminosity functions are estimated at the mean redshift of each redshift interval.

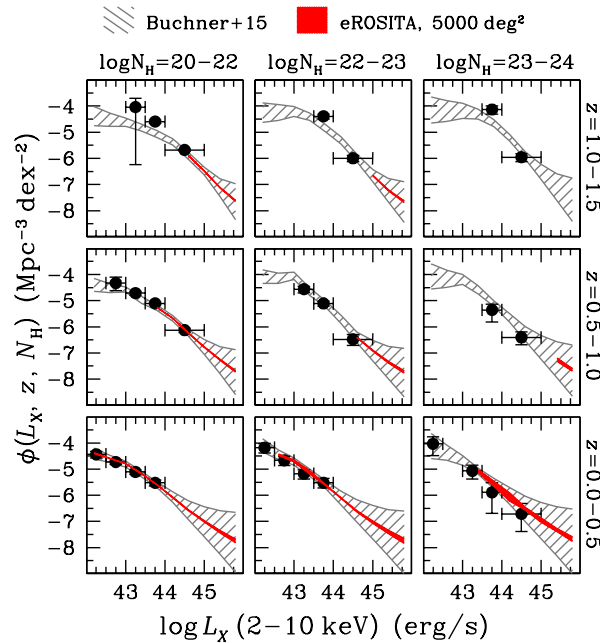


Figure 19. The red shaded regions show the expected constraints on the space density of AGN at different redshift and column density intervals from the eROSITA 4-year observations over a sky area of 5000 deg^2 . The red regions are plotted only for luminosity bins where the expected number of eROSITA detected sources is greater than unity. The black data-points are the constraints from the XMM-XXL-N, the grey hatched area represents the results of Buchner et al. (2015).

Table 3. X-ray AGN space density per luminosity and column density dex in different redshift and $\log N_H$ intervals. The first column lists the logarithm (base 10) of the X-ray luminosity range (2-10 keV band) of each measurement (units of erg/s). The subsequent columns list the logarithm (base 10) of the space density in different $\log N_H$ intervals. For each luminosity bin the median of the logarithmic (base 10) space density is listed. The numbers in the parentheses correspond to the 10th and 90th percentiles of the $\log_{10} \phi$ distributions.

$\log_{10} L_X$	$\log_{10} \phi$ (Mpc $^{-3}$ dex $^{-2}$)			
$z = 0.0 - 0.05$				
	$\log N_H = 20 - 22$	$\log N_H = 22 - 23$	$\log N_H = 23 - 24$	$\log N_H = 24 - 25$
42.0–42.5	-4.43 (-4.57, -4.32)	-4.18 (-4.39, -4.02)	-4.03 (-4.48, -3.76)	–
42.5–43.0	-4.73 (-4.82, -4.64)	-4.67 (-4.86, -4.52)	–	–
43.0–43.5	-5.11 (-5.20, -5.03)	-5.18 (-5.38, -5.02)	-5.07 (-5.38, -4.85)	–
43.5–44.0	-5.52 (-5.65, -5.41)	-5.52 (-5.73, -5.36)	-5.89 (-6.69, -5.51)	-4.95 (-5.48, -4.65)
44.0–45.0	–	–	-6.71 (-7.38, -6.31)	-5.78 (-6.05, -5.58)
45.0–46.0	–	–	–	–
$z = 0.5 - 1.0$				
	$\log N_H = 20 - 22$	$\log N_H = 22 - 23$	$\log N_H = 23 - 24$	$\log N_H = 24 - 25$
42.0–42.5	–	–	–	–
42.5–43.0	-4.33 (-4.62, -4.10)	–	–	–
43.0–43.5	-4.71 (-4.79, -4.64)	-4.56 (-4.70, -4.45)	–	–
43.5–44.0	-5.11 (-5.16, -5.06)	-5.11 (-5.21, -5.03)	-5.36 (-5.81, -5.13)	–
44.0–45.0	-6.13 (-6.22, -6.05)	-6.48 (-6.72, -6.29)	-6.41 (-6.68, -6.20)	–
45.0–46.0	–	–	–	-6.84 (-7.34, -6.53)
$z = 1.0 - 1.5$				
	$\log N_H = 20 - 22$	$\log N_H = 22 - 23$	$\log N_H = 23 - 24$	$\log N_H = 24 - 25$
42.0–42.5	–	–	–	–
42.5–43.0	–	–	–	–
43.0–43.5	-4.04 (-6.24, -3.71)	–	–	–
43.5–44.0	-4.59 (-4.66, -4.53)	-4.39 (-4.50, -4.30)	-4.13 (-4.31, -4.00)	–
44.0–45.0	-5.68 (-5.73, -5.64)	-6.00 (-6.13, -5.89)	-5.96 (-6.13, -5.82)	–
45.0–46.0	–	–	–	-6.85 (-7.34, -6.55)

Table 4. Fraction of obscured (Compton-thin) AGN at different redshift and luminosity intervals. The first column lists the logarithm (base 10) of the X-ray luminosity range (2-10 keV band) of each measurement (units of erg/s). The second column is the obscured fraction. The median of the distribution of the quantity $f = \frac{\int_{20}^{24} \phi(L_X, z, \log N_H) d \log N_H}{\int_{20}^{24} \phi(L_X, z, \log N_H) d \log N_H}$ is listed. The numbers in the parentheses correspond to the 10th and 90th percentiles of the distribution.

$\log L_X$ range	fraction of obscured (Compton-thin) AGN
$z = 0.0 - 0.05$	
42.0–42.5	0.69 (0.55, 0.79)
43.0–43.5	0.50 (0.39, 0.59)
43.5–44.0	0.43 (0.31, 0.54)
$z = 0.5 - 1.0$	
43.5–44.0	0.44 (0.37, 0.50)
44.0–45.0	0.33 (0.25, 0.42)
$z = 1.0 - 1.5$	
43.5–44.0	0.69 (0.63, 0.75)
44.0–45.0	0.34 (0.28, 0.39)

- Stalin C. S., Petitjean P., Srianand R., Fox A. J., Coppolani F., Schwope A., 2010, *MNRAS*, **401**, 294
- Stalin C. S., Srianand R., Petitjean P., 2011, *MNRAS*, **413**, 1013
- Stern D., et al., 2012, *ApJ*, **753**, 30
- Strüder L., et al., 2001, *A&A*, **365**, L18
- Sturm R. K. N., 2012, PhD thesis, Fakultät für Physik, Technische Universität München, Germany
- Surace J. A., Shupe D. L., Fang F., Evans T., Alexov A., Frayer D., Lonsdale C. J., SWIRE Team 2005, in American Astronomical Society Meeting Abstracts. p. 1246
- Sutherland W., Saunders W., 1992, *MNRAS*, **259**, 413
- Tacconi L. J., et al., 2013, *ApJ*, **768**, 74
- Tozzi P., et al., 2006, *A&A*, **451**, 457
- Turner M. J. L., et al., 2001, *A&A*, **365**, L27
- Ueda Y., Akiyama M., Ohta K., Miyaji T., 2003, *ApJ*, **598**, 886
- Ueda Y., Akiyama M., Hasinger G., Miyaji T., Watson M. G., 2014, *ApJ*, **786**, 104
- Vito F., Gilli R., Vignali C., Comastri A., Brusa M., Cappelluti N., Iwasawa K., 2014, *MNRAS*, **445**, 3557
- Worsley M. A., et al., 2005, *MNRAS*, **357**, 1281
- Xue Y. Q., et al., 2010, *ApJ*, **720**, 368
- Xue Y. Q., et al., 2011, *ApJS*, **195**, 10
- Yencho B., Barger A. J., Trouille L., Winter L. M., 2009, *ApJ*, **698**, 380

This paper has been typeset from a $\text{\TeX}/\text{\LaTeX}$ file prepared by the author.